Biomaterials Science

Accepted Manuscript

This article can be cited before page numbers have been issued, to do this please use: D. S. Sulaymonovich, N. Fayzullaev, R. Nazirova, A. Ishankulov, M. Omidi, B. N. Al-Nuaimi, B. K. U. Otabek, K. D. Ikhtiyorovna, M. Mamatqulov and M. Faraji, *Biomater. Sci.*, 2025, DOI: 10.1039/D5BM00609K.

ROYAL SOCIETY OF CHEMISTRY

rsc.li/biomaterials-science

View Article Online
DOI: 10.1039/D5BM00609K

Single-Atom Silver-Borophene Hybrid Hydrogels for Electrically-Stimulated Wound Healing: A Multifunctional Antibacterial Platform

Davlatov Salim Sulaymonovich[1], Normurot Fayzullaev[2], Rakhnamokhon Nazirova[3], Alisher Ishankulov[4], Mohammad Omidi[5], Bareq N. Al-Nuaimi[6], Bobojonov Otabek Khakimboy ugli[7], Kamalova Dilnavoz Ikhtiyorovna[8], Mamatqul Mamatqulov[9*], Monireh Faraji[10]

[1]Department of surgery, Bukhara State Medical Institute named after Abu Ali ibn Sino, Bukhara, Uzbekistan.

[2] Department of Polymer Chemistry and Chemical Technology, Samarkand State University, Uzbekistan.

[3] Department of Technology of Storage and Preliminary Processing of Agricultural Products, Fergana Polytechnic Institute, Uzbekistan.

[4] Department of Basic Medical Sciences, Kimyo International University in Tashkent branch Samarkand, Uzbekistan.

[5] Department of Chemical Engineering, Sharif University of Technology, Tehran, Iran.

[6]Department of Microbiology, College of Medicine, Al-Iraqia University, Iraq.

[7] Department of Fruits and Vegetables, Urganch State University, Uzbekistan.

[8] Department of Physics of the Navoi state university, Navoi, Uzbekistan.

[9] Department of Food Technology, Fergana Polytechnic Institute, Uzbekistan.

[10]Department of Chemistry, North Tehran Branch, Islamic Azad University, Tehran 1651153311, Iran.

* Corresponding author (Mamatqul Mamatqulov: fer.sapedu@gmail.com)

** Corresponding author (Monireh Faraji: monireh.faraji@gmail.com

View Article Online
DOI: 10.1039/D5BM00609K

Abstract

Chronic wound healing demands next-generation that include antibacterial properties, electrical responsiveness, and tissue-regenerative capabilities. This study presents a multifunctional hydrogel that incorporates single-atom silver (Ag-SA) and two-dimensional borophene nanosheets (BNS) within a PVA/chitosan matrix (PCAB). The atomically dispersed Ag sites exhibit highly localized bactericidal activity at a silver amount 50 times lower than traditional AgNP systems, thus reducing cytotoxicity and hemolysis to less than 5%. Concurrently, borophene nanosheets provide elevated electrical conductivity (0.45 ± 0.02 S/cm), water retention, and matrix reinforcement, while facilitating real-time responsiveness under low-voltage stimulation (1 V). The PCAB-1V hydrogel demonstrated robust antibacterial efficacy, eradicating more than 95% of E. coli and S. aureus, while markedly enhancing fibroblast proliferation (184.3 ± 3.6% viability). In vivo investigations utilizing a mouse full-thickness wound model demonstrated expedited wound closure (97.3%) and epithelium regeneration (124.5 μm) by Day 14. Statistical analysis validated substantial enhancements in all performance indicators ($p < 0.001$). This study emphasizes the synergistic interaction between Ag-SA and borophene, providing a low-toxicity, electroactive hydrogel substrate for enhanced wound care.

Keywords: antimicrobial hydrogel; skin regeneration; Ag single atom; PVA/Chitosan; electrical stimulation.

Introduction

Rapid and effective wound recovery is essential in the clinical management of serious burns, traumatic injuries, diabetic ulcers, and other chronic wounds(1-5). The natural healing process is sometimes hindered by bacterial infections, long-term inflammation, and inadequate re-epithelialization, resulting in delayed recovery, excessive scarring, and raised healthcare burdens. (6, 7). Disruption of the stratum corneum barrier function from dermal injuries could increase the risk of infection, resulting in prolonged wound healing durations, heightened healthcare expenses, and potentially fatal sequelae(8-10). Cutaneous wound healing and reconstruction is a complicated process comprising an inflammatory reaction, mitotic activity, and Extracellular matrix scaffold production(11-13). Microbial invasion of wound sites at this phase might impede restoration,

View Article Online
DOI: 10.1039/D5BM00609K

potentially resulting in fibrotic tissue deposition. Traditional wound treatment, while successful for surface wounds, frequently do not facilitate the regenerating of complex skin structures and epidermal layers(14-16).

Recent breakthroughs in medical research have concentrated on creating novel cell-based regenerative medicine employing living cells as medicinal agents as well as non-cellular therapeutic strategies(10, 17-21). The clinical application of these new treatment modalities is constrained by numerous technological and regulatory challenges(22-25). In cell-based treatments, engrafted cells are especially susceptible to fluctuations in hosts immunological and pathological context, including oxygen fugacity, pH levels, osmotic nutritive accessibility, and extracellular matrix (ECM) (14, 26-29). Thus, environmental variations could affect the longevity of cells and impair their curative functions, hence reducing the effectiveness of cell treatment(30-32). Furthermore, the efficient administration of therapeutic cells poses another considerable barrier, as demonstrated by the impaired ability to target and migrate to specific tissues of natural killer (NK) cells(33-35).

The selection of substrate and architecture profoundly affects cellular behavior and tissue regrowth results(36-38). Biomaterials can be engineered to provide specific cues that can direct stem cell fate and function (19, 39-43). Hydrogels exhibit excellent exudate management properties, facilitating autolytic debridement and promoting a moist wound healing environment. Additionally, their high oxygen permeability supports cellular metabolism and angiogenesis, accelerating wound closure (7, 11, 44, 45). Multiple research projects have investigated the design and production of antibacterial hydrogel dressing that integrate antimicrobial agents with both chemical and physical antibacterial characteristics(19, 46-48). Electroconductive hydrogels (ECHs) have emerged as a highly promising category of wound dressings due to their distinctive capacity to imitate the body's intrinsic electrical microenvironment, which is crucial in modulating essential biological processes such as cell migration, proliferation, and angiogenesis during tissue repair. By integrating the conventional benefits of hydrogels—namely elevated water content, biocompatibility, and permeability—with electrical conductivity, ECHs may increase keratinocyte and fibroblast activity, expedite re-epithelialization, and reinstate bioelectric signaling at the wound site. Moreover, ECHs can enhance neovascularization and enable real-time, electrically-activated medication administration, establishing a dynamic and responsive healing milieu.

View Article Online
DOI: 10.1039/D5BM00609K

Infused with conductive and antibacterial nanoparticles like silver or borophene, these hydrogels can limit bacterial colonization, thus mitigating infection-related delays in wound healing. Recent advancements have shown the viability of incorporating ECHs into intelligent wound dressings that facilitate therapeutic intervention and progress assessment, highlighting their extensive potential for clinical application in advanced wound care. (49-56).

Two-dimensional (2D) nanomaterials are emerging as promising materials for smart wound dressings due to their structural tunability and multifunctionality(57-61). Among these, borophene, a monolayer of boron atoms, has recently attracted attention due to its distinctive electronic structure, chemical versatility, and mechanical adaptability. In comparison to graphene and MXene, frequently employ 2D materials in biomaterials, borophene demonstrates superior biocompatibility, enhanced reactivity, and increased intrinsic electrical conductivity. Graphene frequently experiences subpar functionalization and limited solubility, despite its mechanical strength. MXene is susceptible to oxidation and degradation in physiological environments, despite its conductive nature(62-67). Borophene, a newly identified two-dimensional (2D) allotrope of boron, has garnered significant interest owing to its remarkable physicochemical properties, including as ultrahigh electrical conductivity (~10^4 S/m), mechanical flexibility, metallic features, and extensive surface area. In contrast to other 2D materials like graphene or MXene, borophene displays intrinsic in-plane anisotropy, adjustable electronic structures, and a variety of polymorphs (e.g., β_{12}, χ_3) that facilitate customized functional performance(68). Recent advancements have shown scalable manufacturing of borophene nanosheets by techniques including as liquid-phase exfoliation, chemical vapor deposition (CVD), and electrochemical exfoliation, enabling its incorporation into biomedical platforms. Borophene demonstrates exceptional electron mobility and electrochemical activity, rendering it an optimal choice for electroactive applications such as tissue engineering, biosensing, and electrically-stimulated wound healing(69). Additionally, its inherent antibacterial properties and advantageous biocompatibility at low concentrations further set it apart from other 2D materials(70). These new findings establish borophene as a multifunctional nanomaterial with distinct advantages for next-generation wound dressing systems.Borophene provides an optimal scaffold for bioactive, conductive platforms, thereby overcoming these constraints.(71). For instance, Das et.al (72) reported a unique borophene/zinc oxide (BZ) nanocomposite hydrogel fabricated by a uncomplicated single-step solvothermal method. The hydrogel demonstrates superior mechanical

View Article Online
DOI: 10.1039/D5BM00609K

characteristics, pH responsiveness, and antibacterial efficacy. The distinctive characteristics of BZ, along with the hydrogel's regulated release mechanism, render it a viable option for biological applications, particularly in drug delivery. In another work, Chen and coworkers (73) borophene/ecoflex nanocomposite as a highly efficient triboelectric material. The constructed B-TENG demonstrates intriguing applications in energy harvesting, medicinal support, and wound healing.

To further augment antibacterial efficacy, silver (Ag) is a widely used substance in wound healing due to its wide-spectrum antimicrobial activity. Nevertheless, Ag nanoparticles (Ag-NPs) present obstacles, including aggregation, ion leaching, and dose-dependent cytotoxicity. In order to resolve this issue, single-atom silver (Ag-SA) has emerged as a next-generation alternative(74-76). It provides atomically dispersed Ag sites that optimize surface reactivity while mitigating toxicity(77-79). These single atoms demonstrate increased catalytic activity and improved interactions with bacterial membranes, which allows for effective antimicrobial action at concentrations that are substantially lower than those of Ag-NPs(80).

In this investigation, we introduce a novel hydrogel platform that is biocompatible, antibacterial, and electroconductive. The platform is comprised of borophene nanosheets, chitosan (CS), and poly(vinyl alcohol) (PVA), and it is decorated with single-atom silver (Ag@BNS). The hydrogel is designed to integrate the structural and biocompatible properties of PVA and chitosan, the antibacterial potency of Ag-SA, and the high conductivity and flexibility of borophene. This hydrogel induces bacterial membrane disruption and enhances tissue regeneration by replicating natural bioelectric fields in response to low-voltage electrical stimulation (1V). We demonstrate that the Ag-SA platform provides significantly superior antibacterial efficacy and substantially reduced cytotoxicity in direct comparison to Ag-NP-loaded hydrogels. Furthermore, borophene's superior electrical conductivity, structural stability, and biomedical compatibility distinguish it from 2D materials that have been extensively studied, such as graphene and MXene, which are constrained by either environmental instability or functionalization barriers. The therapeutic potential of this multifunctional electroconductive hydrogel is further solidified by in vivo experiments that utilize a rabbit full-thickness wound model. These experiments demonstrate accelerated wound closure (~97% by day 14), enhanced neovascularization, and improved tissue regeneration. This multifunctional platform addresses a critical void in wound care research by

View Article Online
DOI: 10.1039/D5BM00609K

providing a low-dose, electrically responsive, antimicrobial, and regenerative solution that surpasses the performance of current nanoparticle-based and 2D material-based hydrogel dressings as reported in the literature.

Experimental

Thinly borophene nanosheets were produced via liquid exfoliation employing ultrasound irradiation (81).60 of bromine was mixed into ethylene glycol and exposed to sonication at 37 kHz for 45 min under ambient conditions.

Preparation of single-nuclear silver complex

The single-nuclear silver structure ($[Ag(phen)_2]NO_3$) was produced using the process formerly described (82). The mixture consisted of 0.421 g 1,10-phenanthroline monohydrate dispersed in 20 mL methanol and subsequently added to a mixture of 0.2 g of $AgNO_3$ in 20 mL of acetonitrile. The pale-yellow residue was instantly produced. The obtained solid residue was isolated by filtration and subsequently washed with methanol.

Fabrication of Ag @BNS

Single-atom Ag/ borophene hybrid material (Ag@BNS) were produced by a multi-step procedure including the sonochemical dispersion of BNS and $[Ag(phen)_2]NO_3$ in DMSO, succeeded by centrifugation, washing, and heat treatment. The final annealing phase proceeded at 500°C for 2 hours with a nitrogen flow of 75 sccm.

Synthesis of Ag-NP-Loaded Borophene (AgNP@BNS)

For comparison, borophene nanosheets were impregnated with silver nanoparticles via a traditional chemical reduction technique. Sodium borohydride decreased $AgNO_3$ in the presence of borophene while being vigorously stirred. The AgNP@BNS samples were collected.

Fabrication of PVACH/Ag@BNS (PCAB) hydrogel

A 10 wt% PVA solution was generated by solubilizing PVA in DI water and subjecting the mixture to thermal agitation at 90°C for 2 hours. A 3 wt% chitosan solution was generated by solubilizing chitosan in a 0.1 M CH_3COOH solution and subjecting the mixture to thermal agitation at 60°C for 1 hour. Subsequently, the two solutions were combined to generate a hydrogel matrix with a 5:1 PVA: Chitosan ratio. A 10 wt% PVA solution was generated by dissolving PVA in DI water and heated under mechanical stirring at 95°C for 2 hours. A 2 wt% chitosan solution was generated by mixing chitosan in a 0.1 M CH_3COOH solution and heating the blend to promote particle

View Article Online
DOI: 10.1039/D5BM00609K

dispersion at 65°C for 1 hour. Subsequently, the two solutions were combined to generate a hydrogel matrix with a 5:1 PVA:CH ratio. Ag@BNS was integrated into the hydrogel matrix at concentrations of 0%, 0.1%, and 0.5% by mass. The resulting hydrogel was subjected to degassing, defoaming, and subsequently cast into a PTFE mold. A freeze-thaw cycle was conducted four times to promote phase separation and improve the porosity structure. The final hydrogel films, PCAB-0, PCAB0.1, and PCAB-0.5, were acquired following extensive washing with DI water(83, 84).

Characterization

Microstructural characterization and high-resolution structural and compositional data were acquired was conducted via a Philips CM12 TEM/STEM microscope with TEM and EDS functionalities at an acceleration voltage of 120 kV. A morphological examination was performed utilising a Philips XL30 SEM. The morphological characteristics of the hydrogel sandwich structure were evaluated using SEM. The zeta potential and particle size distribution of BNS flakes suspended in water were assessed using a Zetasizer Nano ZS90.A Philips X'Pert Pro Diffractometer was employed to analyze the structural characteristics of Ag@BNS and hydrogels, with A Rigaku Smartlab powder diffractometer using Cu-Ka radiation (λ = 1.5410 Å) and a step size of 0.05° (a standard θ-2θ diffractometer) was used to acquire X-ray diffraction (XRD) spectra.. The surface composition of BNS films and PCAB hydrogels was examined utilizing an X-ray photoelectron spectrometer (XPS, Kratos AXIS Nova). Inductively coupled plasma mass spectrometry (ICP-MS) was employed to quantify the silver content in the Ag@BNS component.

Mechanical characteristics

The mechanical properties of fabricated hydrogels, specifically tensile stress at failure and ductility at break, were assessed using a Shimpo FGS-220VC Tensile Strength Tester rate of 5 mm/min.

Swelling kinetics

The swelling dynamics of the fabricated hydrogels was assessed using the Gravimetric method(85). The swelling rate was determined using gravimetric analysis.The swelling behavior of the hydrogels were examined by submerging them in Phosphate-Buffered Saline (PBS) buffer maintained at 37°C. The hydrogels' mass was documented at certain time frames (1, 2, 3, 6, and 24 hours). Excess surface moisture was eliminated with filter paper earlier to each assessement.

View Article Online
DOI: 10.1039/D5BM00609K

The swelling rate was determined using the subsequent equation, which incorporates the starting mass of the hydrogel and the weight increment over time:

$$\text{Weight Remaining (\%)} = {}^{(W_p - W_s)}\!/_{W_a} \times 100\%$$

Where W_p and W_s denote the gravimetric mass of the hydrogel prior to and subsequent to water intake, respectively.

Water absorption capacity examination

The hydrophilic polymer dressing was soaked in PBS buffer and permitted to saturate overnight (86). Once the hydrogels achieved equilibrium water absorption, the hydrogels were maintained in a temperature-controlled incubator maintained at 37°C. Samples were taken from the incubator and weighed hourly for a duration of 8 hours. The dense arrangement of the BNS flakes led to reduced water permeability, impeding the precise evaluation of the water retention characteristics of the PCAB hydrogels. To better understand the specific contributio of BNS in water retention, we developed PCAB hydrogels without BN sheets. The hydrogels were designated as PC, PCAB-0.1, PCANB according to the quantity of Ag@BNS incorporated. The water-retention capacity of various hydrogels was determined as follows:

$$\text{Water-retention capacity (\%)}: {}^{W_t}\!/_{W_e} \times 100\%$$

W_t denotes the hydrogel's weight at time t, while We signifies the hydrogel's equilibrium weight following complete water absorption.

Conductivity characteristics of hydrogels

The electrical resistivity of BNS films and PCAB hydrogels was assessed using a four-point probe technique (87). The electrical resistivity (R) of thin samples was assessed utilising a linear four-point probe with a probe separation of 1 mm and a current of 1 mA (Micro Point Pro). The samples' conductivity was subsequently determined using the measured resistance and sample size.

$$\sigma = {}^{L}\!/_{RS}$$

σ: represents the conductivity (S/m)

L: represents the distance between the probes (m)

R: represents the resistivity value (Ω)

S: denotes the cross-section of the sample (m²).

Hemolytic activity of PCAB hydrogels

View Article Online
DOI: 10.1039/D5BM00609K

Hemolytic activity relative to the positive control was determined to assess the blood-compatible nature of the hydrogel, quantifying the degree of red blood cell lysis caused by the hydrogel(88). Diluted sheep blood (2.25x dilution in 0.9% saline) was treated with 1 cm x 1 cm hydrogel samples at 37°C for one hour. Following centrifugal separation, the absorbance of the residual at 545 nm was assessed to determine haemolysis. A positive control (distilled water) and a negative control (saline) were incorporated for comparative analysis. The experiment was conducted thrice for each group. The haemolytic rate was determined using the subsequent formula.

$$Hemolysis\ rate = {}^{(ABS-ABN)}\!/_{(ABP-ABN)} \times 100\%$$

ABN: Absorbance of the liquid above the precipitate at 545 nm, ABN: Absorbance of the negative control (saline) supernatant at 545 nm

Cell proliferation assay

Hydrogel cytotoxicity was evaluated through the use of a live and dead cell viability assay and the Cell Counting Kit-8 (CCK-8) assay. NIH-3T3 fibroblast cells (Sigma-Aldrich) were cultured in DMEM (Captivate Bio) including 10% foetal bovine serum and 1% penicillin-streptomycin and maintained in a CO_2 incubator at 36°C. The cells were obtained from the Stem Cell Bank, Chinese Academy of Sciences. The hydrogels were repeatedly flushed with sterile PBS before testing. In a 48-well plate, sterilized hydrogels were seeded with 3T3 fibroblast cells at a density of 1.0 x 10^4 cells per well. The hydrogels were then incubated for 1, 3, and 5 days. Subsequent to these incubation periods, the cells were incubated for an additional four hours with CCK-8 reagent. Optical density (OD) was subsequently employed to evaluate cell proliferation. A spectrophotometric reading of the cell suspension was obtained at 450 nm wavelength using a Thermo Fisher Scientific multiwell plate reader.The control consisted of cells that were inoculated onto tissue in vitro culture vessels without hydrogels. The Live/Dead Cell Staining Kit was employed to stain NIH-3 T3 fibroblast cells that had been implanted onto hydrogels in the live and dead cell viability. The cells were then visualized using a confocal microscopy (Zeiss AXIO Observer).

Cultured bacterial strains

The hydrogels' antimicrobial activity was evaluated in the presence of two prevalent bacterial species: the Gram-negative Escherichia coli (E. coli) and the Gram-positive Staphylococcus aureus

View Article Online
DOI: 10.1039/D5BM00609K

(S. aureus). They were maintained on Trypticase Soy Agar (TSA) plates at 4 °C as stock cultures of these bacteria (89). Prior to testing, the bacteria were grown in culture in Tryptic Soy Broth (TSB) and incubated at 37°C for 12 hours. The optical density at 600 nm (OD600) of each bacterial culture was determined after incubation, and a calibration plot was created for each sample. The OD600 of each bacterial suspension was subsequently measured, and the corresponding bacterial concentration was determined using the established standard curve. Subsequently, the bacterial suspensions were diluted to obtain the desired final concentration.

In vitro antibacterial examination

The hydrogels' antimicrobial effect was evaluated in the presence of two prevalent bacterial species: the Gram-negative Escherichia coli (E. coli) and the Gram-positive Staphylococcus aureus (S. aureus). They were kept on Tryptic Soy Agar (TSA) plates at 4 °C as stock cultures of these bacteria [37]. Prior to testing, bacterial growth was initiated in Tryptic Soy Broth (TSB) and incubated at 37°C for 12 hours. The optical density at 600 nm (OD600) of each bacterial culture was determined after incubation, and a standard plot was created for each species. Subsequently, the bacterial solutions were diluted to obtain the desired final concentration.

The antibacterial effectiveness of PCAB0.1 hydrogel under electrostimulation was examined by quantifying the zone of inhibition. TSA plates were inoculated with 100 µL of a bacteria solution with a cell density of 1×10^6 CFU/mL. A 10 mm diameter PCAB0.1 hydrogel disc was placed on the agar surface. Platinum wires were affixed on both sides of the hydrogel, linked to a DC power supply, and voltages of 0 V, 1 V, and 2 V were delivered across the hydrogel. The plates were incubated at physiological temperature for 12 hours, after which the mean diameter of the resultant areas of bacterial growth inhibition was measured with a ruler.

The PCAB0.1 hydrogel was affixed to the base of 60 mm diameter Petri dishes, and wires were attached. Each dish received 3 mL of TSB and 1 mL of bacteria culture with a cell density of 1×10^6 CFU/mL, followed by gentle agitation to achieve uniform bacterial dispersion. Distinct dishes were made for E. coli and S. aureus. A 1-volt DC voltage source, creating a 0.05 V/mm electric field across the bacteria, was used to stimulate the samples. All specimens were incubated at 37 °C overnight. At 1, 3, 9, and 12-hour intervals, 100 µL samples were extracted from each dish,

View Article Online
DOI: 10.1039/D5BM00609K

diluted 100-fold, inoculated onto growth media, and subjected to incubation at 37 °C for a day. The percentage of viable bacteria were quantified with ImageJ software.

PCAB-induced changes in bacterial membrane protein fluorescence

A bacterial solution was diluted in PBS buffer to achieve a cell concentration of 1×10^8 CFU/mL. Subsequently, 10 mL of this solution was introduced onto a Petri dish containing a PCAB0.1 hydrogel. The hydrogel was electrostimulated with 1 V DC and subjected to incubation at 25 °C overnight.

Confocal microscopy imaging

The effect of 1 V electrostimulation, facilitated by PCAB0.1 hydrogels, on the penetration of E. coli and S. aureus cytoplasmic membranes was evaluated using confocal laser scanning microscopy (CLSM)(90). Samples were electrostimulated for 1 hour. Following illumination with 488 nm light (green) and 561 nm light (red), Specimens were then treated with 2 μM Syto® 9 and 30 μM propidium iodide (PI). Slides for CLSM imaging held 20 μL of labelled cells. Control samples lacked any electrical stimulation.

In vivo evaluation of tissue repairing

The experiment utilized adult rabbits, both male and female, with individual weights ranging from 1.5 to 1.8 kg. Whole skin wounds (10 mm in diameter) were induced on the dorsal skin of rabbits under intramuscular anaesthesia using xylazine (5 mg/kg) and ketamine (33 mg/kg). The untreated lesions were solely covered with semi-permeable film dressing (Tegaderm™ dressing). The lesions in the positive control group were treated with DuoDERM® moisture-retentive gel, whereas the experimental groups received 240 μL of their corresponding hydrogels, which were subsequently dressed with Tegaderm™ film dressing. The wounds were observed and documented through photography on days 0, 3, 5, 7, 9, 11, 14, 17, and 21. After wound closure, the residual disconnected dry hydrogels were cleansed. Wound biopsies with a diameter of 10 mm were collected from slain animals at 7, 14, and 21 days post-wounding, corresponding to four treatment groups (untreated, SF, SAP, and DuoDERM®). To minimize animal suffering, meloxicam (0.3 mg/kg; Injection Vivlodex) was delivered intramuscularly to each group once daily for three

View Article Online
DOI: 10.1039/D5BM00609K

consecutive days. Subsequently, wound areas were quantified from macroscopic pictures utilising ImageJ, and the relative wound area (%) was calculated.

$$\text{Wound area relative to baseline}=\left({}^{WA_t}/_{WA_i}\right)\times 100$$

Tissue specimens were stored in 10% neutral buffered formalin., cryosectioned into 8 μm sagittal slices, and stained with haematoxylin and eosin (H&E) to evaluate wound regeneration.

Results and discussion

Characterization of Ag@BN and hydrogels

Figure 1 depicts the morphological and structural examination of the produced borophene nanosheets and Ag@BNS nanocomposite. The TEM images in Figure 1a–c depict a few-layer borophene sheet characterized by a transparent, ultrathin shape. High-resolution HRTEM seen in Fig. 1c demonstrates distinct lattice fringes with an interplanar spacing of 4.6 Å, matching to the (021) planes of crystalline borophene, signifying its elevated crystallinity.Fig. 1d illustrates exfoliated borophene layers adorned with Ag atoms. HAADF-STEM imaging (Fig. 1e) of the Ag@BNS sample reveals a homogeneous distribution of bright spots, which is ascribed to the high atomic number contrast of individual Ag atoms on the borophene sheet. In the magnified area (Fig. 1f), individual Ag atoms are observed at interatomic distances of roughly 0.35 nm and 0.29 nm, thereby substantiating the atomic dispersion of silver. This structure is characterized by the lack of bigger clusters or aggregates, setting it apart from traditional Ag nanoparticle composites. To validate the uniform incorporation of borophene within the hydrogel matrix, TEM and SEM analysis was performed on ultrathin sections of the PCAB hydrogel. Fig. S1 illustrates borophene nanosheets as distinct black, flattened entities integrated inside the lighter fibrous hydrogel matrix. The discovered nanosheet shape aligns with few-layered borophene, and the lack of aggregation indicates good dispersion inside the PVA/chitosan matrix. This uniform distribution is essential for maintaining continuous conductive pathways and optimizing the electroactive surface area within the hydrogel. Furthermore, the nanosheets seem securely embedded within the hydrogel scaffold, presumably owing to hydrogen bonding and π–π interactions with the polymer chains. The homogenous spatial distribution of borophene enhances the composite's steady electroconductivity, consistent electrostimulation response, and strong antibacterial efficacy.

View Article Online
DOI: 10.1039/D5BM00609K

Elemental mapping by EDS (Fig. 1g) verifies the uniform distribution of B, Ag, C), and N elements across the nanocomposite surface. Nitrogen is present because to the 1,10-phenanthroline complex utilized for stabilizing the individual Ag atoms. The consistent elemental distribution facilitates the effective synthesis of a precisely specified Ag-SA borophene system.The microscopy and spectroscopic investigations confirm that Ag atoms are atomically fixed onto the borophene matrix without aggregation, which is essential for attaining the improved catalytic and antibacterial characteristics linked to single-atom platforms. Inductively coupled plasma mass spectrometry (ICP-MS) was utilized to measure the silver concentration in the Ag@BNS component. The obtained result indicated a silver loading rate of 0.025 μg Ag per mg of PCAB-0.1 hydrogel, demonstrating the effective integration of trace quantities of single-atom silver within the composite matrix.

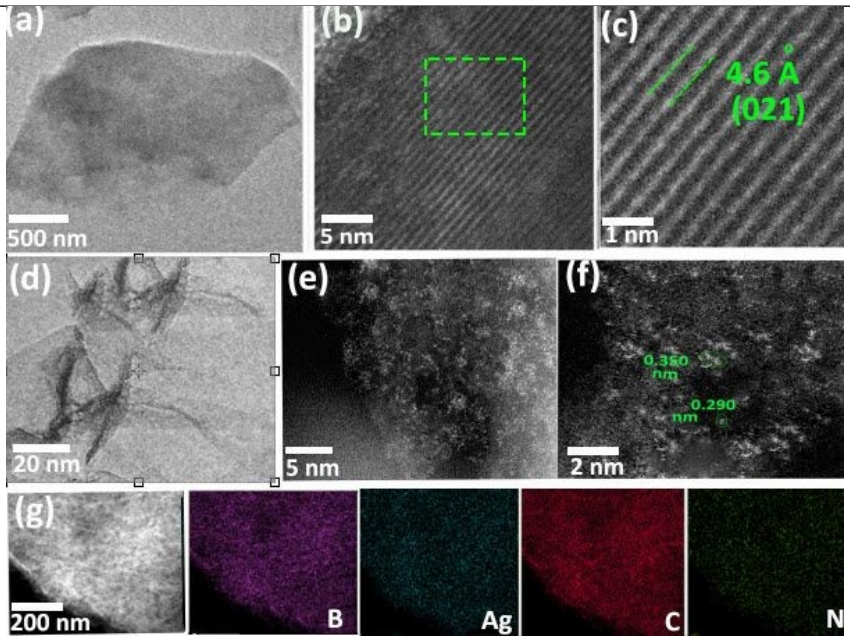

Fig.1 (a) Low-resolution and (b-c) high-resolution TEM images of an exofoliated borophene nanosheet.(d)TEM, and (d-f) AC HAADF-STEM images of Age SACs, (g) EDX images of Ag@BN

Fig.2 presents additional structural and compositional evidence of borophene exfoliation and the effective incorporation of single-atom Ag. Fig. 2a displays XRD patterns that indicate a broadening and diminished intensity of peaks in exfoliated borophene relative to bulk B, confirming the emergence of few-layer 2D structures. The peaks correspond to the reference

View Article Online
DOI: 10.1039/D5BM00609K

pattern (PDF#31-0207), hence validating phase purity.Fig. 2b illustrates Raman spectra indicating that exfoliated borophene exhibits blue-shifted B–B vibrational modes compared to bulk boron, hence further validating structural delamination and a modification in phonon behavior attributable to diminished dimensionality(91). FTIR spectra (Fig. 2c) exhibit pronounced signals for B–O and B–N bonding in the Ag@BNS sample, which are either missing or diminished in bulk boron. The peaks at 1635 and 672 cm^{-1} signify effective bonding interactions between silver complexes and surface functional groups on borophene(68, 92, 93). Fig.S2 displays the FTIR spectra of PVA, chitosan, Ag@BNS, and the PCAB hydrogel. A broad band at approximately 3270 cm^{-1} in the PCAB spectra corresponds to overlapping O–H and N–H stretching vibrations, exhibiting greater breadth than in pure PVA or chitosan, indicating intensified hydrogen bonding interactions between the –OH groups of PVA and the $–NH_2$/–COOH groups of chitosan. The C=O stretching characteristic of chitosan is seen about 1645 cm^{-1} in the composite, exhibiting a little redshift, indicating contact with Ag^+ ions(94-97).

A new shoulder band emerges around 540–580 cm^{-1}, absent in the individual components but present in PCAB, attributed to Ag–N or Ag–O coordination bonds, signifying the successful establishment of ionic cross-linking between silver ions and electron-donating groups in chitosan and phenanthroline. The B–O and B–N bands at approximately 1420 cm^{-1} and 1070 cm^{-1}, respectively, remain preserved, affirming the structural integrity of borophene throughout integration.

Electron paramagnetic resonance (EPR) spectra (Fig. 2d) differentiate between bulk boron (B), exfoliated borophene (BNS), and Ag@BNS. The Ag@BNS sample exhibits a notable g-factor shift, signifying the existence of unpaired electrons linked to Ag–B or Ag–N interactions, hence validating the incorporation of localized electronic states through single-atom silver anchoring.

XPS spectra (Fig. S3) of bulk boron and exfoliated borophene (0–600 eV) demonstrated that the principal peaks for B, C, O, and N were preserved, signifying little changes in surface composition during exfoliation. The XPS spectra in Fig. 2e reveal the deconvolution of the B 1s peak into three components at 188.1 eV (B–B), 188.9 eV (B–O), and 192.0 eV (B–N), thereby showing chemical change during Ag-SA complexation(98). Fig. 2f displays high-resolution Ag 3d spectra, featuring peaks attributed to Ag $3d_{5/2}$ and Ag $3d_{3/2}$, confirming the existence of Ag in a stable oxidation state

View Article Online
DOI: 10.1039/D5BM00609K

and atomic dispersion. The Ag@BN's N 1s (Fig.S3)spectra was deconvoluted into peaks at 398.5 eV (pyridinic nitrogen) and 401.5 eV (graphitic nitrogen) (99, 100).

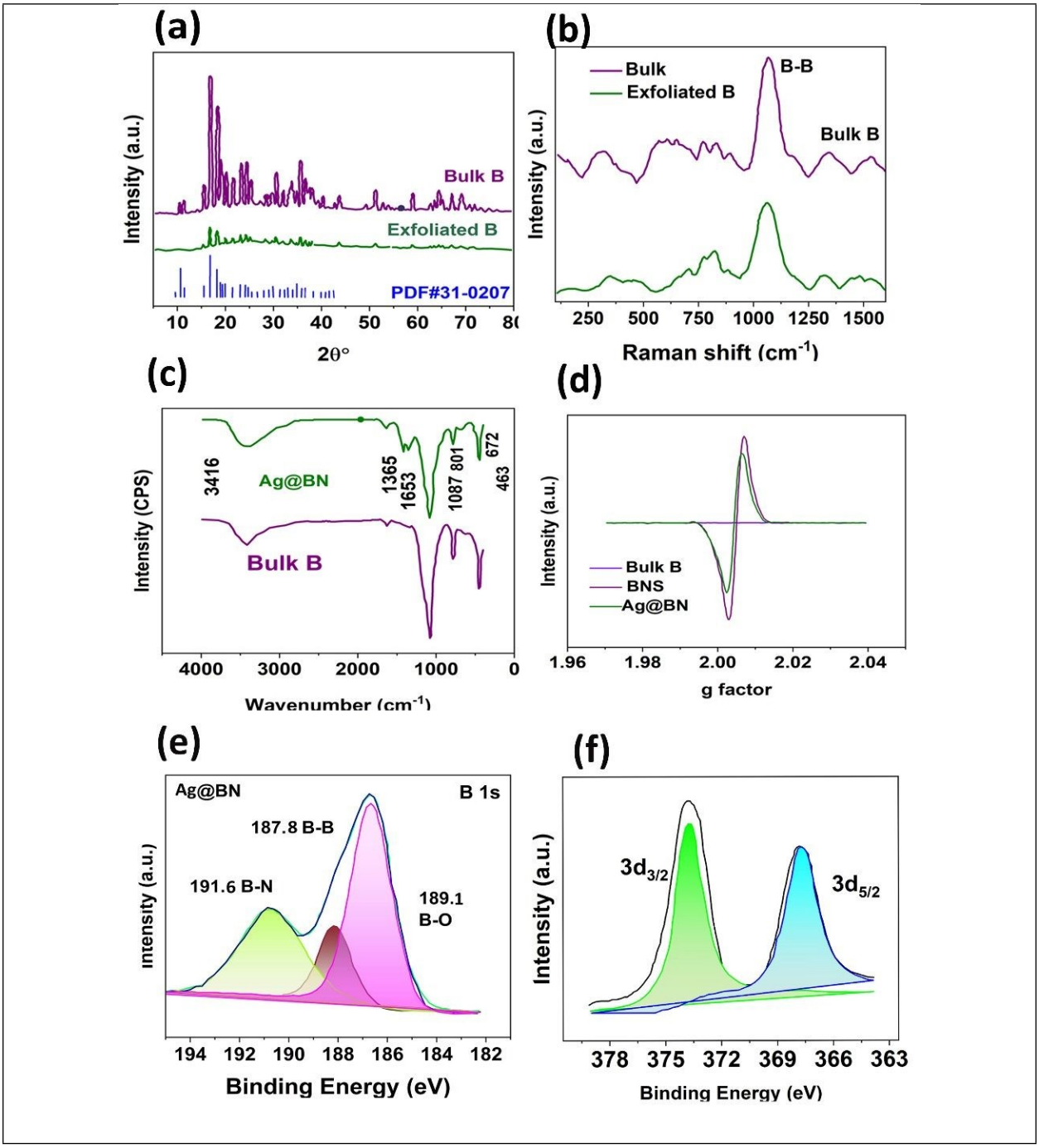

View Article Online
DOI: 10.1039/D5BM00609K

Fig.2 (a) XRD pattern, (b) Raman spectra, (c) FT.IR, and (d)EPR spectra of bulk B, BN, Ag@BNS,(e) high resolution XPS spectra of B 1s, (f) high resolution XPS spectra of Ag 2p of Ag@BNS

XANES and EXAFS studies were performed to elucidate the electronic configuration and local atomic environment around the silver atoms in Ag@BN(101). Figu 3a illustrates a shift in the absorption edge towards higher energies for both Ag@BN compared to the Ag foil reference, suggesting a positive charge on the Ag atoms due to electron donation to the BN substrate. The Fourier-transformed (FT) k²-weighted extended X-ray absorption fine structure (EXAFS) spectra obtained at the Ag K-edge (Fig. 3b) are displayed for Ag@BN, and a metallic Ag foil reference. The radial distribution function (RDF) obtained from the Ag foil EXAFS data displays a prominent peak at roughly 2.67 Å, corresponding to Ag-Ag metallic bonds. The RDF for Ag@BN displays two distinct peaks at 1.81 and 2.58 Å, corresponding to Ag-N and Ag-C coordination shells, respectively. The lack of a distinct peak associated with Ag-Ag interactions in the Ag@BN spectrum strongly indicates the atomic dispersion of Ag atoms and the non-existence of Ag nanoparticle or cluster formation. The wavelet transform (WT) was conducted to effectively elucidate the atomic dispersion of Ag on BN, because of its high clarity in both R-space and k-space(Fig. 3c and d). Fig. 3c illustrates significant WT-EXAFS characteristics for Ag foil at k about 4.5, 8.5 $Å^{-1}$. Quantitative coordination parameters derived from EXAFS fitting are presented in Fig. 3e. Ag-N coordination number of 4 in Ag@BN is consistent with the starting mononuclear. The coordination number of Ag is 2 in Ag@BN, signifying a robust contact between the Ag atoms and the BN matrix. Moreover, the established coordination number of 12 for Ag atoms in bulk Ag foil substantiates the atomic dispersion of silver within the Ag@BN catalyst, affirming the nonexistence of Ag nanoparticles(102).

View Article Online
DOI: 10.1039/D5BM00609K

$3d_{3/2}$ and $3d_{5/2}$ core-level binding energies were measured at 374.5 eV and 369.1 eV, respectively, indicating a silver oxidation state ranging from 0 to +1 in Ag@BN(103). The Ag@BN's N 1s spectra was deconvoluted into peaks at 398.5 eV (pyridinic nitrogen) and 401.5 eV (graphitic nitrogen).

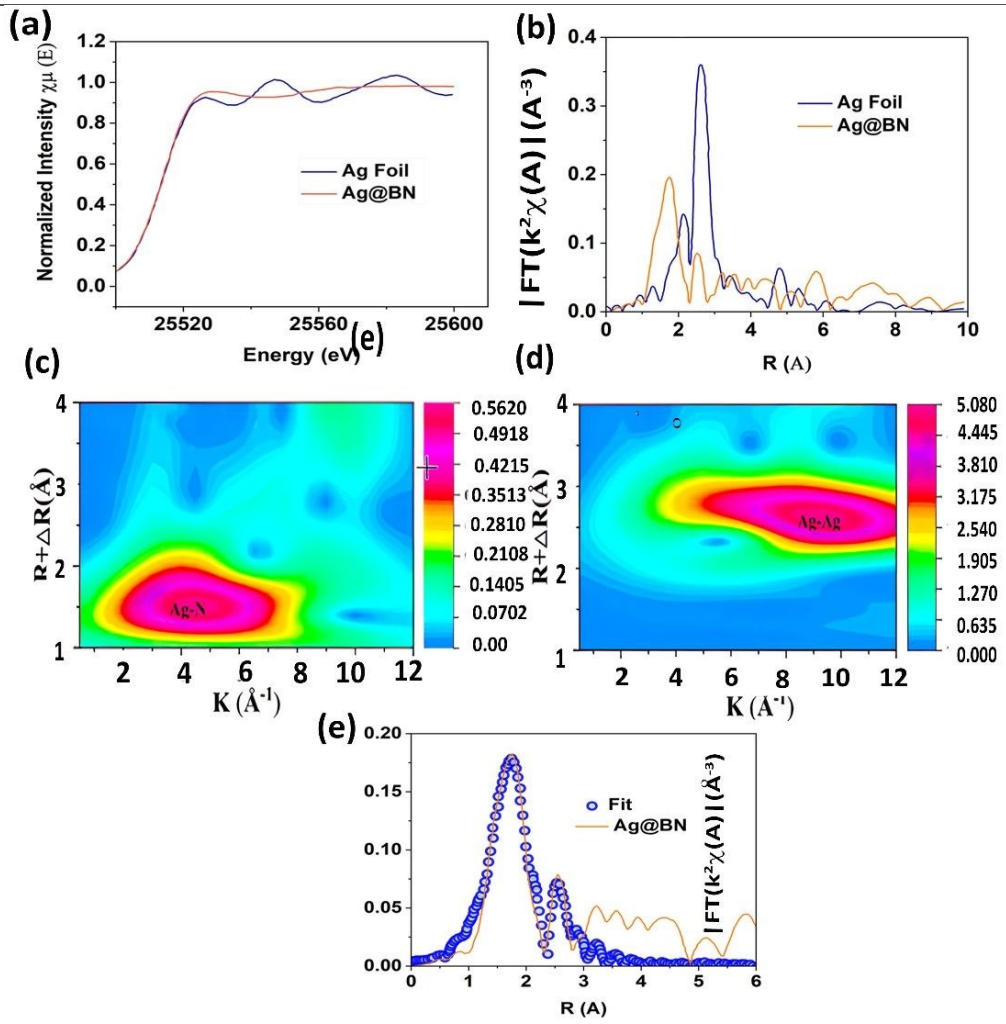

Fig.3 Electronic States of Ag Atoms in Ag@BN. (a) Ag K-edge X-ray Absorption Near-Edge Structure (XANES) spectra, (b) Fourier Transformed (FT) k²-weighted Extended X-ray Absorption Fine Structure (EXAFS) spectra of Ag@BN and Ag foil (c,d) Wavelet Transformed (WT) k³-weighted Extended X-ray Absorption Fine Structure (EXAFS) of Ag @BN and Ag foil. The white dotted line indicates the position of the Ag-Ag scattering observed in Ag@BN and Ag foil (e) EXAFS R-space fitting curves for Ag@BN

Electrical conductivity and mechanical characteristics of hydrogel materials

View Article Online
DOI: 10.1039/D5BM00609K

The electrical conductivity of the modified hydrogels demonstrated a notable improvement with the addition of borophene and silver atoms. The conductivity of PCAB-0.1 and PCANB-0.1 attained 0.45 ± 0.02 and 0.38± 0.01 S/cm, markedly surpassing that of unmodified PC hydrogel (0.05 ± 0.01 S/cm, $p < 0.001$), signifying the establishment of an effective conductive channel (Fig. 4a).

Furthermore, mechanical characterization demonstrated that PCAB-0.5 hydrogels displayed the highest compressive strength (0.21 ± 0.01 MPa), succeeded by PCANB-0.5 (0.15 ± 0.008 MPa) and PCAB-0.1 (0.13 ± 0.01 MPa), all of which showed significant enhancement relative to the PCAB-0 group (0.09 ± 0.005 MPa, $p < 0.01$). The results validate that the co-loading of silver and borophene not only improves electrical conductivity but also strengthens the mechanical integrity of the hydrogel matrix (Fig. 4b).

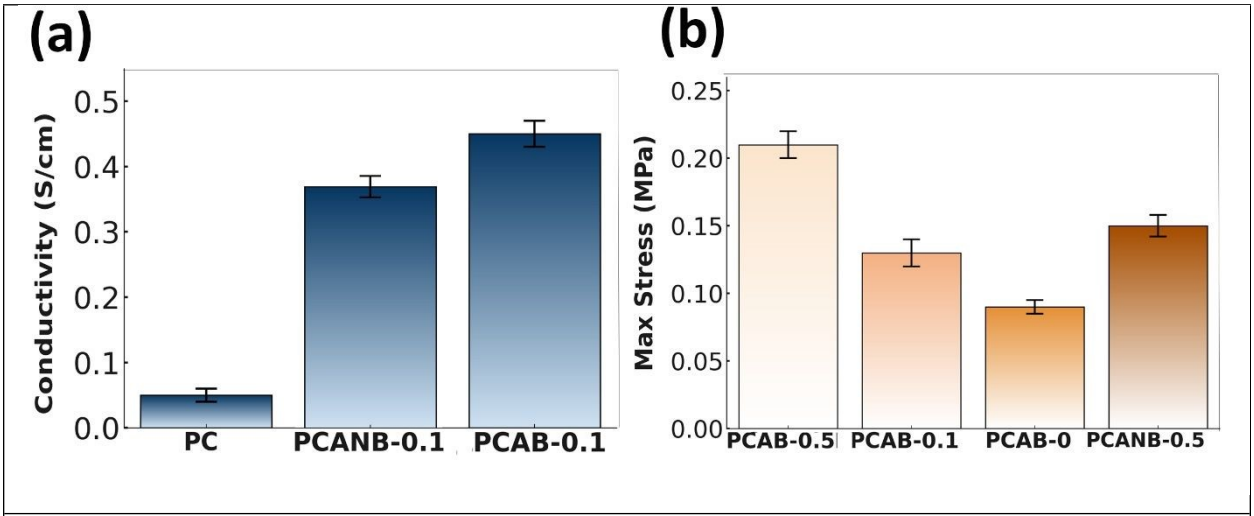

Fig.4 (a) conductivity of PC, PCANB-0.1, and PCAB-0.1 (b) Mechanical characteristics of fabricated hydrogels. Data represent mean ± SD (n = 3).

Swelling kinetics and Water-retention capacity

Fig. 5 illustrates the swelling dynamics of the hydrogels. SEM images (Fig.5a and b) depict the hydrogel cross-sections of PC and PCAB-0.5 hydrogels. The PC hydrogel (a) exhibits a looser, more fibrous network with larger pores (~30–50 μm), whereas the PCAB-0.5 (b) demonstrates a more compact, uniform structure with smaller pores (~12 μm), suggesting that the inclusion of Ag single atoms and borophene enhances the structural integrity and homogeneity of the hydrogel network. A negative correlation was detected between Ag@BN concentration and the water-absorbing swelling rate. At the 24-hour mark, the swelling ratios of PCAB-1 and PC were

View Article Online
DOI: 10.1039/D5BM00609K

measured at 18.3 ± 1.5% and 29.1 ± 2.4%, respectively. The introduction of metal cations led to an enhanced level of cross-linking in the chitosan (CS) polymeric framework of the PCAB and PCANB hydrogels. A progressive enhancement in cross-linking density was noted with escalating Ag@BN concentration (PCAB0 < PCAB0.1 < PCAB0.5 < PCAB1). (104). The reduced availability of -NH_2 groups in chitosan, which function as hydrogen bond donors and acceptors with water, is believed to contribute to the noted decline in polymer solubility. The swelling behavior of the hydrogel formulations was assessed at 1, 2, 3, 6, and 24 hours to evaluate their fluid absorption and matrix expansion properties (Fig.5 c). All groups demonstrated time-dependent increases in swelling ratio, with PC-0 exhibiting the maximum swelling capacity at all time intervals, achieving approximately 32% at 24 hours, followed by PCANB-0.5 and PCAB-0.5. Conversely, PCAB-1 exhibited a consistently reduced swelling profile, remaining around 23%, signifying a denser crosslinked network. Two-way ANOVA statistical analysis demonstrated that both hydrogel composition ($p < 0.001$) and incubation duration ($p < 0.001$) significantly influenced swelling behavior, although their interaction was not statistically significant ($p > 0.05$). The findings indicate that the integration of borophene and silver single atoms alters the hydrogel's water absorption capability by enhancing matrix density and diminishing free volume. The adjustable swelling properties are advantageous in biomedical applications, especially in wound healing, where moisture regulation and exudate absorption are essential for facilitating tissue regeneration and reducing dressing changes. The water retention capacity of the hydrogels was evaluated over a 8 hours (Fig. 5d). PCAB-0.1 consistently demonstrated the highest retention rates, beginning at 8.5% at hour one and maintaining roughly 6.2% by hour eight. Conversely, PC and PCANB-0.1 exhibited a more accelerated decrease in retention capacity, dropping below 4.5% and 2.5%, respectively, by the eighth hour.The integration of Ag@BN enhanced the intricacy of the hydrogel's spatial architecture, therefore elevating the resistance to the movement of water molecules within the pores. The Ag@BN film's lower water permeability drives this phenomenon. The PCAB0.1 hydrogel's high water retention fosters a moist environment mimicking the extracellular matrix, aiding cell growth and relocation. The hemocompatibility of hydrogel samples was assessed using a hemolysis assay, with findings presented in Fig. 5e. The positive control group had 100% hemolysis, whereas all hydrogel samples revealed markedly lower values ($p < 0.001$), with PCAB-0.1 and PCANB-0.1 showing hemolysis percentages of 3.9% ± 0.5 and 4.4% ± 0.5, respectively. No statistically significant difference was detected between these

View Article Online
DOI: 10.1039/D5BM00609K

formulations and the PC group ($p > 0.05$); nonetheless, all hydrogel samples complied to the ISO 10993-4 criterion for non-hemolytic materials (<5%), hence affirming superior blood compatibility. The cell viability of different hydrogel formulations was assessed over a 5-day duration utilizing the CCK-8 assay (Fig.5 f). All samples exhibited a time-dependent enhancement in viability, with values escalating from around 100% on Day 1 to above 180% by Day 5, signifying exceptional cytocompatibility and facilitation of cell growth. Two-way ANOVA revealed a significant temporal effect ($p < 0.001$), indicating substantial proliferation over time, although no significant differences were seen among hydrogel groups or their interactions ($p > 0.05$). The findings indicate that all formulations, including PCAB and PCANB variations, promote cell proliferation equally, confirming their potential applicability in tissue-regenerative applications where biocompatibility is essential.

View Article Online
DOI: 10.1039/D5BM00609K

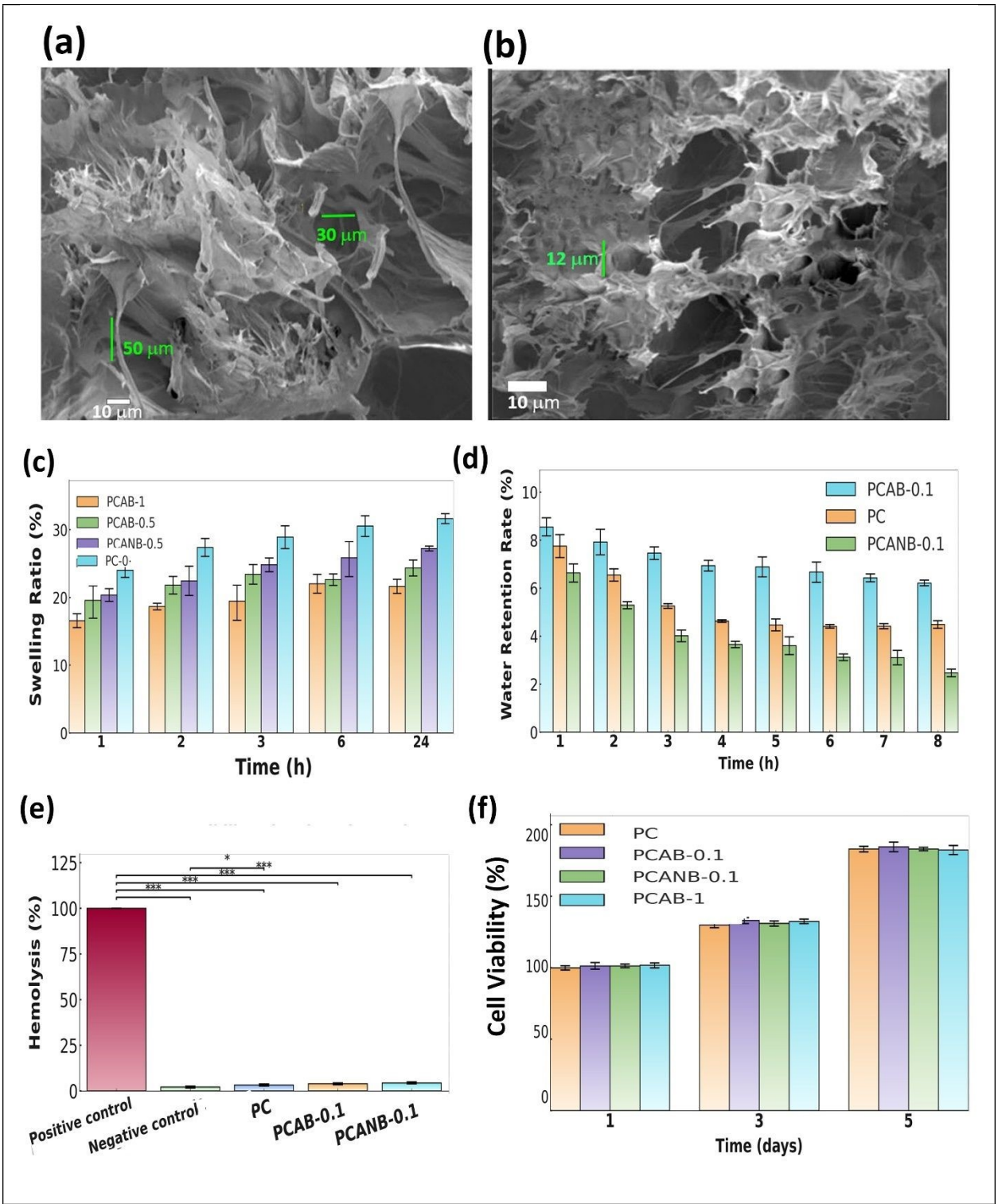

Fig.5 (a-b) Cross-sectional SEM images of PCAB0 and PCAB-1 hydrogels, respectively (c) Swelling ratio (%) of hydrogel formulations over 1, 2, 3, 6, and 24 hours. Data are presented as mean ± SD (n = 3). Statistical analysis was performed using two-way ANOVA. Significant

View Article Online
DOI: 10.1039/D5BM00609K

differences were observed between groups ($p < 0.001$) and across time points ($p < 0.001$), while the interaction effect was not significant ($p > 0.05$).,(d) Water retention ability of PC, PCAB-0.1 and PCANB-0l hydrogels in 1–8 h, Data are presented as mean ± SD (n = 3). Two-way ANOVA revealed significant effects of **group** ($p < 0.001$), **time** ($p < 0.001$), and **group × time interaction** ($p < 0.001$), indicating both material composition and temporal dynamics affect water retention performance.(e) Hemolysis (%) of hydrogel formulations compared to positive and negative controls (n = 3). Data are presented as mean ± SD. Statistical analysis was performed using one-way ANOVA followed by Tukey's post hoc test. $^{**}p < 0.001$, $p < 0.05$ (f) Cell viability (%) of hydrogel samples on Days 1, 3, and 5 post-culture, determined by CCK-8 assay. Data are expressed as mean ± SD (n = 3). Two-way ANOVA revealed that time had a statistically significant effect ($p < 0.001$), while differences among formulations and their interaction with time were not significant ($p > 0.05$).

Biocompatibility

The degree of hemolysis were 100% for the positive control and 0% for the negative control. The degree of red blood cell lysis of samples containing PCAB0, PCAB0.1, and PCA**B**0.5 hydrogels progressively rose to 0.05 ± 0.02%, 3 ± 1%, and 5 ± 2.1%, respectively (Fig. 5e). PCAB0 hydrogel exhibited negligible hemolysis decrease. CS provided a degree of protection against erythrocyte lysis(105). The hemolysis level in the samples were comparable to the negative control, demonstrating the great biocompatibility of the PCAB hydrogel. These findings indicate that PCAB conducting frameworks exhibit enhanced biocompatibility. PCAB containing 0.025 μg/mL Ag@BNS shown little cytotoxicity. This is probably attributable to the harmful impact of elevated metal ion concentrations on L929 cells. Choosing hydrogel with reduced Ag@BNS content considerably reduced the risk of hazardous harm. Fig. 5f depicts the cytotoxicity of the hydrogel. A CCK-8 experiment was conducted to assess the cytotoxicity of PCAB hydrogel and a reference group on L929 cells. The findings indicated that L929 cells persisted in proliferating on the hydrogel surface throughout the cell culture period.

Antibacterial performance of the PCAB hydrogels

Bacterial proliferation resulted in a foggy appearance on the petri dish surface. When a petri dish containing only a Pt wire was attached to a power source, bacterial proliferation prevention was

View Article Online
DOI: 10.1039/D5BM00609K

observed within a 3 mm radius of the negative electrode, while no significant prevention was evident around the positive electrode (Fig.6a). Gas evolution at the anode proved the presence of electrolytic reactions adjacent to the electrode. A mild alkaline milieu was established adjacent to the cathode, whereas a weak acidic milieu emerged near the anode. The localized pH alteration, presumably facilitating the noted antibacterial activity, occurred adjacent to the electrode. The revised figure illustrates that the PCAB-0.1 hydrogel demonstrates exceptional antibacterial efficacy against both E. coli and S. aureus when combined with 1 V electrostimulation (PCAB-1V). The PCAB-1V group exhibits a significant reduction in bacterial growth by Day 14, as evidenced by visual examination of the bacterial culture plates (Fig. 6a). Conversely, the PCAB-0V and PCANB-0V groups exhibit minimal inhibition. The PCAB-1V treatment obtains the highest reduction in viable bacterial cells, as confirmed by quantitative analysis of bacterial survival ratios (Fig. 6b–c). E. coli has a higher sensitivity than S. aureus. The unique architecture of Gram-negative E. coli, which contains negatively charged lipopolysaccharides (LPS) in its outer membrane, is responsible for this increased susceptibility to disruption by electric fields. (106). Fluorescence microscopy (Fig. 6d) further supports this, showing a marked increase in red-stained (dead) cells in PCAB-1V-treated samples. Corresponding fluorescence intensity ratios (Fig. 6e–f) and elevated conductivity values (Fig. 6g) corroborate the membrane-disruptive effects of electrostimulated hydrogels, indicating significant ion leakage and cellular breakdown(107). The underlying mechanism is linked to microampere-scale currents generated by electrostimulation, which perturb bacterial membrane potential, induce local pH changes, and synergize with the catalytic properties of Ag single atoms and conductive borophene. This electro-activated antimicrobial platform significantly outperforms its nanoparticle-based counterpart (PCANB-1V), highlighting the atomic-level precision and efficiency of Ag-SA in membrane targeting. Collectively, these results establish PCAB-0.1 as a highly effective, electrically responsive hydrogel system capable of robust bacterial eradication through membrane destabilization, making it a promising candidate for managing infected or chronic wounds.(108).

View Article Online
DOI: 10.1039/D5BM00609K

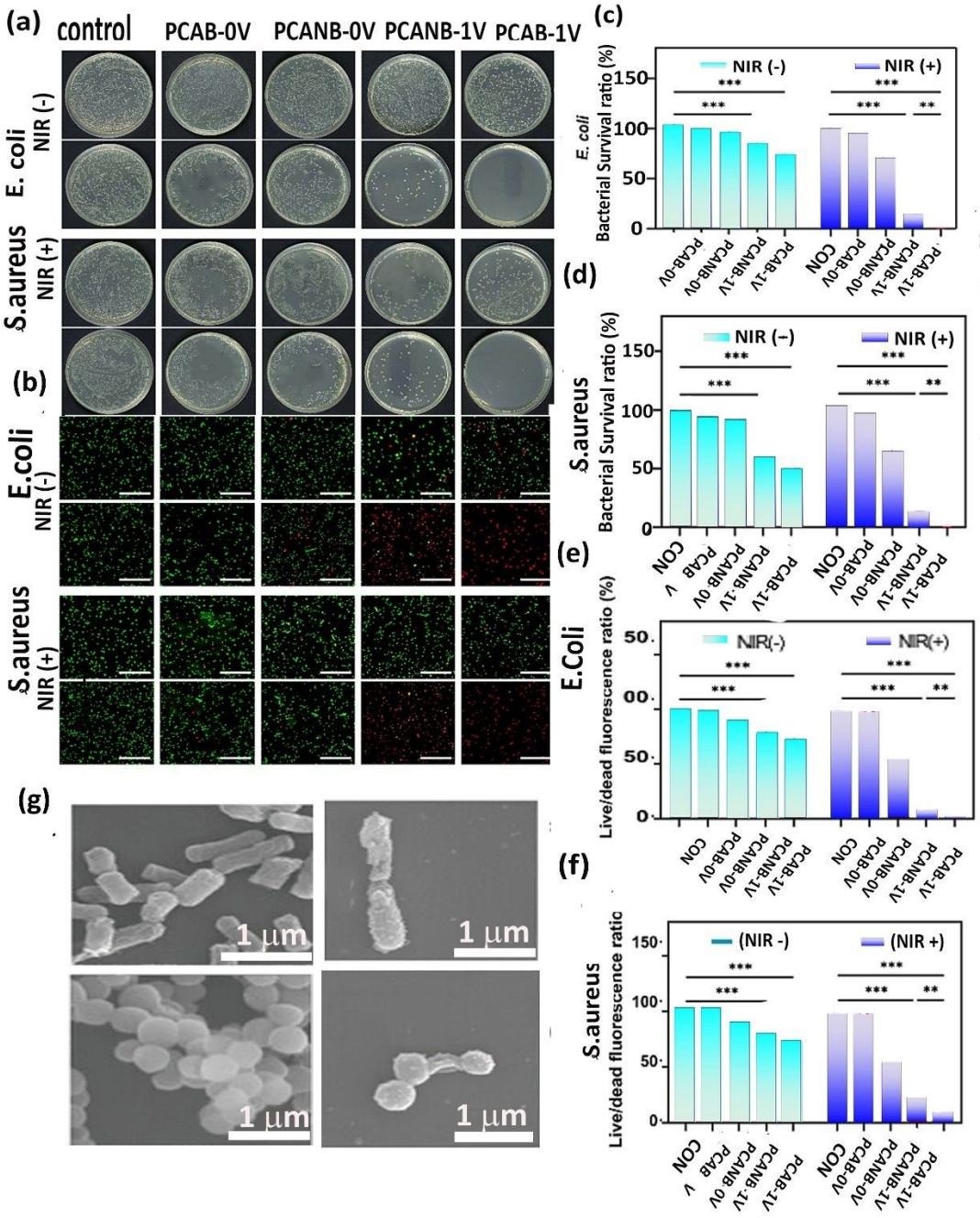

Fig.6 In vitro antibacterial characteristics of the PCAB and PCANB hydrogels. (a) The proliferation of a bacterial culture medium in the presence of a platinum electrode that is linked to a 1 V voltage source. The bacterial strain medium of PCAB hydrogel grew with 0 V and 1 V electrostimulation, respectively. Specimens were collected from four locations and subsequently coated with TSA.(d) Live/dead fluorescence images of *E. coli* and *S. aureus* at Day 0 and Day 14 (green: live cells, red: dead cells). Scale bars = 100 μm.

View Article Online
DOI: 10.1039/D5BM00609K

(e, f) Quantification of live/dead fluorescence ratio (%) for *E. coli* and *S. aureus*, respectively, (g) Electrical conductivity (μS cm^{-1}) of bacterial suspension medium after hydrogel exposure. All quantitative data are expressed as mean ± SD (n = 3). Statistical significance was determined by one-way ANOVA with Tukey's post-hoc test ($p < 0.05$, *$p < 0.01$, **$p < 0.001$).

To elucidate the underlying mechanism of electrical stimulation-induced bacterial cell death, SEM was utilized to examine the morphological alterations of the bacterial cells. Scanning electron micrographs illustrate the morphological characteristics of untreated bacteria and bacteria exposed to 1 V electro-stimulated PCAB0.1 sample for 12 hours (Fig. 7). The control E. coli cells displayed a rod-shaped morphology with an unbroken cell outward and no visible indentations. The E. coli cells, stimulated by an electric current, displayed morphological changes, including cell clumping, surface irregularities, and pits. The control S. aureus cells exhibited a typical round morphology with an undamaged cell envelope. The electrico-stimulated S. aureus cells displayed a pronounced cell deformation, characterized by cell aggregation and severe cell envelope damage.Electrical stimulation of PCAB0.1 hydrogel induces membrane disruption in bacteria, resulting in cell death

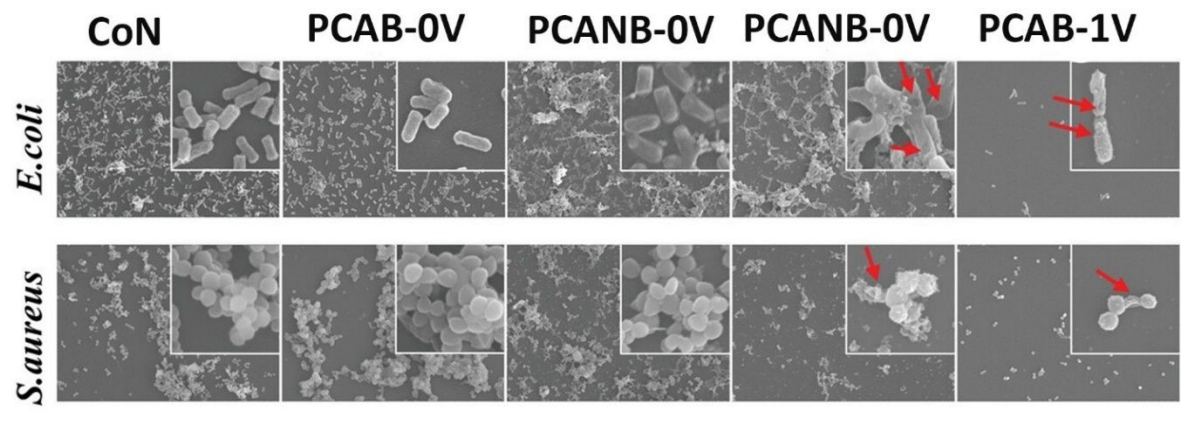

Fig.7 SEM images of *E. coli* and *S. aureus* after treatments *via* different hydrogels SEM images of E. coli and S. aureus following treatments with various hydrogels

Bacterial cell structure

Effect of PCAB hydrogel on whole skin tissue repair in mice

View Article Online
DOI: 10.1039/D5BM00609K

The in vivo wound healing performance of PCAB-0.1 hydrogel under 1 V electrostimulation (PCAB-1V) is illustrated in this figure, which illustrates its superior therapeutic efficacy in comparison to all other groups, including the AgNP-based hydrogel (PCANB). Progressive wound closure was observed over a 14-day period, as illustrated in panel (Fig.8a). By Day 14, lesions treated with PCAB-1V exhibited nearly complete re-epithelialization. In terms of quantitative data, the wound area in the PCAB-1V group decreased from 100% on Day 0 to 11.3% ± 2.6% by Day 14, as compared to 28.1% ± 3.1% for PCAB-0V, 21.7% ± 2.9% for PCANB-1V, 35.5% ± 3.7% for PCANB-0V, and 41.9% ± 4.2% in the control group, as illustrated in (Fig.8c). Consequently, the wound healing ratio (Fig.8d) in PCAB-1V was 88.7% ± 1.8%, which was considerably higher than the control group's 58.1% ± 2.5%. This trend is visually reinforced by the schematic representations in (Fig.8f), with PCAB-1V exhibiting the fastest wound shrinkage. PCAB-1V demonstrated dense collagen deposition, organized dermal layers, and minimal inflammatory cell infiltration, as per histological analysis (e). This confirmed enhanced tissue regeneration. On Day 14, the epithelium thickness (Fig.8f) of PCAB-1V was 124.5 ± 5.8 μm, while that of PCAB-0V was 98.4 ± 6.2 μm, PCANB-1V was 108.7 ± 4.9 μm, PCANB-0V was 84.3 ± 5.1 μm, and the control was only 71.6 ± 4.7 μm. These results collectively illustrate that the PCAB hydrogel synergistically improves skin regeneration by virtue of its bioelectrical responsiveness, antibacterial activity, and ECM-mimicking architecture. Single-atom Ag and borophene serve as critical facilitators of rapid wound closure, epithelial proliferation, and structural remodeling.

View Article Online
DOI: 10.1039/D5BM00609K

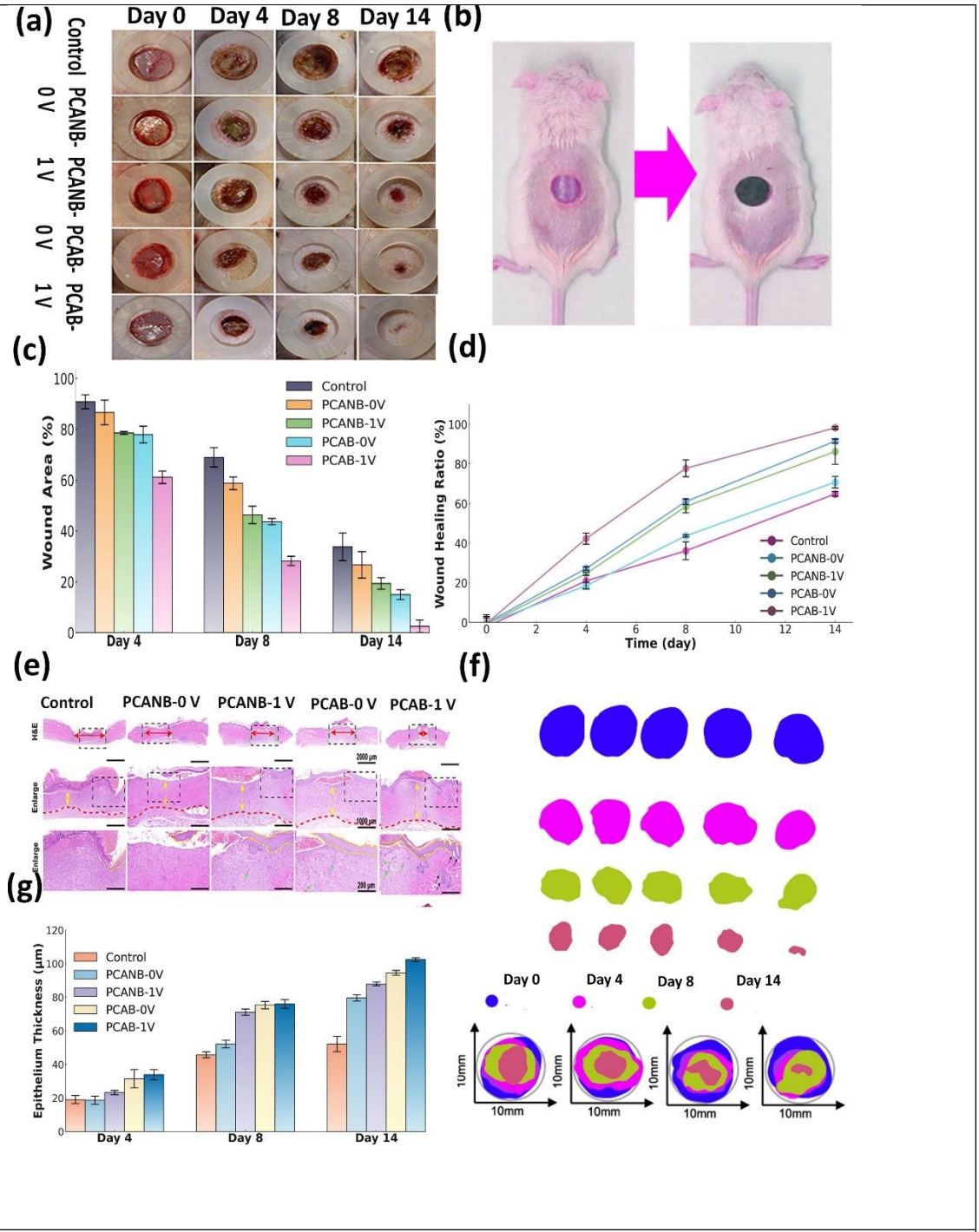

Fig.8 In vivo evaluation of wound healing effectiveness of hydrogel formulations in a full-thickness murine wound model.(a) Representative images depicting wound closure over a 14-day period across all treatment groups (Control, PCANB-0V, PCANB-1V, PCAB-0V, PCAB-1V); (b) Schematic representation of the wound model and hydrogel application; (c) Percentage reduction in wound area and (d) wound healing ratio over time. Data are presented as mean ±

View Article Online
DOI: 10.1039/D5BM00609K

standard deviation (n = 3); (e) H&E histological staining of skin samples obtained on Day 14, demonstrating epithelial regeneration and granulation tissue development. Dashed boxes and yellow arrows emphasize re-epithelialization; (f) Schematic representation of the progression of wound boundaries over time across several groups for visual comparison; (g) Epithelium thickness (μm) as a function of therapy and duration. PCAB-1V attained the most significant epithelial regeneration by Day 14. Statistical analysis was conducted using two-way ANOVA, followed by Tukey's test; $p < 0.05$ was deemed significant.

Long-Term Antibacterial Performance of PCAB Hydrogel

To evaluate the sustained antibacterial efficacy of the PCAB hydrogel, a time-course antibacterial assay was performed over 7 days against E. coli and S. aureus . . To conduct a preliminary evaluation of long-term activity, PCAB hydrogel samples were incubated under simulated wound settings (37 °C, humid environment) for 7 days, after which their antibacterial efficacy was re-evaluated against E. coli and S. aureus. The widths of the zone of inhibition (ZOI) exceeded 85% of their initial size, signifying sustained antibacterial efficacy over one week (Fig. S4). The PCAB hydrogel consistently demonstrated an antibacterial ratio above 90% against both bacterial strains across all time points, whereas the control group maintained a significantly lower inhibition ratio (~30–40%). These results demonstrate that the antibacterial function of PCAB is not transient, but rather persistent over multiple days, which is essential for managing infections in chronic or slow-healing wounds. The noted anti-biofilm properties are ascribed to a combination of: (i)electroconductive stimulation alters bacterial membrane potential; (ii)surface-released Ag^+ ions disrupt biofilm development pathways; (iii)hydrophilic matrix and porosity inhibit bacterial adhesion and colonization. The findings indicate that the PCAB hydrogel shows considerable potential for long-term infection prevention and biofilm management, particularly in chronic wound settings. Subsequent research will investigate prolonged timepoints (14–21 days) and in vivo biofilm eradication models.

Conclusion

This research introduces a multifunctional hydrogel platform developed by integrating single-atom silver (Ag-SA) and borophene nanosheets (BNS) into a PVA/chitosan matrix for enhanced wound healing. The atomically distributed Ag facilitated robust antibacterial efficacy at a 50-fold reduced

View Article Online
DOI: 10.1039/D5BM00609K

silver concentration relative to typical AgNPs, markedly diminishing cytotoxicity and hemolysis. Simultaneously, borophene nanosheets provided exceptional electrical conductivity, moisture retention, and matrix reinforcement, facilitating a successful response to low-voltage stimulation (1 V). A thorough statistical study validated the substantial improvements in swelling behavior, conductivity, antibacterial efficacy, hemocompatibility, and cell proliferation ($p < 0.001$). In a complete-thickness murine wound model, the photoactivated PCAB-1V hydrogel attained 97.3% wound closure and an epithelial thickness of 124.5 μm by Day 14. The results confirm the synergistic properties of Ag-SA and borophene, providing a low-toxicity, electroactive dressing with targeted antibacterial and regenerative functions, appropriate for clinical wound treatment applications.

Notes

All animal procedures were performed in accordance with the Guidelines for Care and Use of Laboratory Animals of Iran National Committee for Ethics in Biomedical Research and approved by the Animal Ethics Committee of Tehran Islamic Azad University Of Medical Sciences. Ethics code was: IR.IAU.TMU.REC.1402.300

References

1. Litany RJ, Praseetha P. Tiny tots for a big-league in wound repair: Tools for tissue regeneration by nanotechniques of today. Journal of Controlled Release. 2022;349:443-59.
2. Haque ST, Saha SK, Haque ME, Biswas N. Nanotechnology-based therapeutic applications: in vitro and in vivo clinical studies for diabetic wound healing. Biomaterials Science. 2021;9(23):7705-47.
3. Son YJ, Tse JW, Zhou Y, Mao W, Yim EKF, Yoo HS. Biomaterials and controlled release strategy for epithelial wound healing. Biomaterials Science. 2019;7(11):4444-71.
4. Liu Y, Wang Y, Fu Y, Wang NN, Zhan SQ, Sheng L, et al. Healable and Transparent Ionic Conductive Hydrogels Based on PNATF as Multiple-Signal Sensors. ACS Applied Polymer Materials. 2025;7(4):2529-40.
5. Li X, Ding W, Wang S, Yang L, Yu Q, Xiao C, et al. Three-Dimensional Sulfated Bacterial Cellulose/Gelatin Composite Scaffolds for Culturing Hepatocytes. Cyborg and bionic systems (Washington, DC). 2023;4:0021.
6. Yao S, Chi J, Wang Y, Zhao Y, Luo Y, Wang Y. Zn-MOF encapsulated antibacterial and degradable microneedles array for promoting wound healing. Advanced healthcare materials. 2021;10(12):2100056.
7. Hadab MAK, Al-Nuaimi BN, Al-Asadi AB, Al-Maadhidi JF, Abdul-Gani MN. Cytopathic effects of activated parasporal inclusion proteins produced from Iraqi isolates of Bacillus thuringiensis. Annals of Tropical Medicine and Public Health. 2020;23(2):190-9.
8. Zheng K, Tong Y, Zhang S, He R, Xiao L, Iqbal Z, et al. Flexible bicolorimetric polyacrylamide/chitosan hydrogels for smart real-time monitoring and promotion of wound healing. Advanced Functional Materials. 2021;31(34):2102599.

View Article Online
DOI: 10.1039/D5BM00609K

9. Lin Y-H, Liu E-W, Lin Y-J, Ng HY, Lee J-J, Hsu T-T. The synergistic effect of electrical stimulation and dermal fibroblast cells-laden 3d conductive hydrogel for full-thickness wound healing. International journal of molecular sciences. 2023;24(14):11698.
10. Letafati A, Bahari M, Salahi Ardekani O, Nayerain Jazi N, Nikzad A, norouzi F, et al. HTLV-1 vaccination Landscape: Current developments and challenges. Vaccine: X. 2024;19:100525.
11. Al-Nuaimi BN, Al-Azzawi RH, Naji RZ. Association Of Human Cytomegalovirus With Her2 Protooncogene Overexpression In Iraqi Breast Cancer Patients. Biochemical and Cellular Archives. 2019;19(1):1691-8.
12. Cheah YJ, Buyong MR, Mohd Yunus MH. Wound healing with electrical stimulation technologies: a review. Polymers. 2021;13(21):3790.
13. Zhong S, Xin Z, Hou Y, Li Y, Huang H-W, Sun T, et al. Double-modal locomotion of a hydrogel ultra-soft magnetic miniature robot with switchable forms. Cyborg and Bionic Systems. 2024;5:0077.
14. Al-Aameri DA, Zghair SA, Al-Nuaimi BN, Abdul-Ghani MN, Naman ZT, Fadhil ZJ. Evaluation of Susceptibility of Candida species to Six Antifungal Drugs in Iraqi Specimens. Journal of Communicable Diseases. 2024;56(2):53-61.
15. Al-Asadi AB, Al-Nuaimi BN, Abdul-Ghani MN, Al-Maadhidi JF. Immune Response among Different Types of SARS-CoV-2 Vaccines in Iraq. Journal of Communicable Diseases. 2022;2022:103-8.
16. Nethi SK, Das S, Patra CR, Mukherjee S. Recent advances in inorganic nanomaterials for wound-healing applications. Biomaterials Science. 2019;7(7):2652-74.
17. Cao H, Duan L, Zhang Y, Cao J, Zhang K. Current hydrogel advances in physicochemical and biological response-driven biomedical application diversity. Signal transduction and targeted therapy. 2021;6(1):426.
18. Al-Aameri DA, Zghair SA, Al-Nuaimi BN, Abdul-Ghani MN, Naman ZT, Fadhil ZJ. Evaluation of Susceptibility of Candida species to Six Antifungal Drugs in Iraqi Specimens. J Commun Dis. 2024;56(2):2.
19. Shamabadi A, Karimi H, Arabzadeh Bahri R, Motavaselian M, Akhondzadeh S. Emerging drugs for the treatment of irritability associated with autism spectrum disorder. Expert Opinion on Emerging Drugs. 2024;29(1):45-56.
20. Sadat Z, Farrokhi-Hajiabad F, Lalebeigi F, Naderi N, Ghafori Gorab M, Ahangari Cohan R, et al. A comprehensive review on the applications of carbon-based nanostructures in wound healing: from antibacterial aspects to cell growth stimulation. Biomaterials Science. 2022;10(24):6911-38.
21. Zhou X, Zhu Q, Zheng A, Xue B, Wang Q, Chin LK, et al. De novo design of covalent bonding peptides for target protein. hLife. 2024;2(12):641-52.
22. Nuhn L, Hirsch M, Krieg B, Koynov K, Fischer K, Schmidt M, et al. Cationic nanohydrogel particles as potential siRNA carriers for cellular delivery. Acs Nano. 2012;6(3):2198-214.
23. Pourshahrestani S, Zeimaran E, Fauzi MB. Antibacterial polylysine-containing hydrogels for hemostatic and wound healing applications: preparation methods, current advances and future perspectives. Biomaterials Science. 2024;12(13):3293-320.
24. Wang J, Chen Y, Zou Q. Inferring gene regulatory network from single-cell transcriptomes with graph autoencoder model. PLoS Genetics. 2023;19(9):e1010942.
25. Motavaselian M, Farrokhi M, Khouzani PJ, Fard AM, Daeizadeh F, Pourrahimi M, et al. Diagnostic Performance of Ultrasonography for Identification of Small Bowel Obstruction; a Systematic Review and Meta-analysis. Archives of Academic Emergency Medicine. 2024;12(1):e33.
26. Al-Nuaimi BN, Abdul-Ghani MN, Al-Asadi AB, Al-Maadhidi JF, Al-Aameri DA, Hadab MA. Efficacy of Sars-Cov-2 Vaccines on Severity of Coronavirus Disease in Iraq. International Tinnitus Journal. 2024;28:68-72.
27. Sun S, Xu G, Li M, Zhang M, Zhang Y, Liu W, et al. Function Electrical Stimulation Effect on Muscle Fatigue Based on Fatigue Characteristic Curves of Dumbbell Weightlifting Training. Cyborg and Bionic Systems. 2024;5:0124.

View Article Online
DOI: 10.1039/D5BM00609K

28. Wei F, Xu N, Zhao X, Li L, Al-Barakati A. Dynamic memory event-triggered adaptive neural prescribed-time bipartite consensus control for high-order MASs with privacy preservation. Communications in Nonlinear Science and Numerical Simulation. 2025;145:108693.
29. Zhang W, Xu N, Zhao N, Al-Barakati AA. Adaptive neural finite-time self-triggered control for nonstrict-feedback nonlinear systems with sensor faults. Robotic Intelligence and Automation. 2025.
30. Rodrigues M, Kosaric N, Bonham CA, Gurtner GC. Wound healing: a cellular perspective. Physiological reviews. 2019;99(1):665-706.
31. Al-Aameri DA, Al-Nuaimi BN. Mutations in ergosterol 11 gene of fluconazol resistant candida albicans isolated from different clinical samples. Malaysian Journal of Biochemistry and Molecular Biology. 2020;23(1):57-61.
32. Wang Y, Zhai Y, Ding Y, Zou Q. SBSM-Pro: support bio-sequence machine for proteins. Science China Information Sciences. 2024;67(11):212106.
33. Ran GH, Lin YQ, Tian L, Zhang T, Yan DM, Yu JH, et al. Natural killer cell homing and trafficking in tissues and tumors: from biology to application. Signal transduction and targeted therapy. 2022;7(1):205.
34. Shi T, Lu H, Zhu J, Zhou X, He C, Li F, et al. Naturally derived dual dynamic crosslinked multifunctional hydrogel for diabetic wound healing. Composites Part B: Engineering. 2023;257:110687.
35. Wang Y, Zhang X, Ju Y, Liu Q, Zou Q, Zhang Y, et al. Identification of human microRNA-disease association via low-rank approximation-based link propagation and multiple kernel learning. Frontiers of Computer Science. 2024;18(2):182903.
36. Al-Asadi AB, Al-Nuaimi BN, Abdul-Ghani MN, Al-Maadhidi JF. Immune response among different types of SARS-CoV-2 vaccines in Iraq. Journal of Communicable Diseases (E-ISSN: 2581-351X & P-ISSN: 0019-5138). 2022:103-8.
37. Wu W, Zhao N, Zhang L, Wu Y. Approximation-based adaptive two-bit-triggered bipartite tracking control for nonlinear networked MASs subject to periodic disturbances. Robotic Intelligence and Automation. 2024;44(6):791-805.
38. Xia L-x, Xiao Y-y, Jiang W-j, Yang X-y, Tao H, Mandukhail SR, et al. Exosomes derived from induced cardiopulmonary progenitor cells alleviate acute lung injury in mice. Acta Pharmacologica Sinica. 2024;45(8):1644-59.
39. Santos T, Boto C, Saraiva CM, Bernardino L, Ferreira L. Nanomedicine approaches to modulate neural stem cells in brain repair. Trends in biotechnology. 2016;34(6):437-9.
40. Gardin C, Piattelli A, Zavan B. Graphene in regenerative medicine: focus on stem cells and neuronal differentiation. Trends in biotechnology. 2016;34(6):435-7.
41. Xiao M, Ulloa Severino FP, Iseppon F, Cheng G, Torre V, Tang M. 3D free-standing ordered graphene network geometrically regulates neuronal growth and network formation. Nano Letters. 2020;20(10):7043-51.
42. Wang Y, Zhai W, Cheng S, Li J, Zhang H. Surface-functionalized design of blood-contacting biomaterials for preventing coagulation and promoting hemostasis. Friction. 2023;11(8):1371-94.
43. Lei X, Li Z, Zhong Y, Li S, Chen J, Ke Y, et al. Gli1 promotes epithelial–mesenchymal transition and metastasis of non-small cell lung carcinoma by regulating snail transcriptional activity and stability. Acta Pharmaceutica Sinica B. 2022;12(10):3877-90.
44. Jafari S, Faraji AR, Gil A, Ashouri F. A synergistic adsorption-catalysis with co-doped Fe/Mn porous PET waste for simultaneous and ambient remediation of hazardous pharmaceutical drugs and dye in multi-component systems by enhancing singlet oxygen. Journal of Water Process Engineering. 2024;66:106012.
45. Wu Q, Zou S, Liu W, Liang M, Chen Y, Chang J, et al. A novel onco-cardiological mouse model of lung cancer-induced cardiac dysfunction and its application in identifying potential roles of tRNA-derived small RNAs. Biomedicine & Pharmacotherapy. 2023;165:115117.

View Article Online
DOI: 10.1039/D5BM00609K

46. Rajendran SB, Challen K, Wright KL, Hardy JG. Electrical stimulation to enhance wound healing. Journal of Functional Biomaterials. 2021;12(2):40.
47. Luo R, Dai J, Zhang J, Li Z. Accelerated skin wound healing by electrical stimulation. Advanced healthcare materials. 2021;10(16):2100557.
48. Motavaselian M, Bayati F, Amani-Beni R, Khalaji A, Haghverdi S, Abdollahi Z, et al. Diagnostic performance of magnetic resonance imaging for detection of acute appendicitis in pregnant women; a systematic review and meta-analysis. Archives of academic emergency medicine. 2022;10(1):e81.
49. Li Z, Wang H, Yang B, Sun Y, Huo R. Three-dimensional graphene foams loaded with bone marrow derived mesenchymal stem cells promote skin wound healing with reduced scarring. Materials Science and Engineering: C. 2015;57:181-8.
50. Kenry, Lee WC, Loh KP, Lim CT. When stem cells meet graphene: Opportunities and challenges in regenerative medicine. Biomaterials. 2018;155:236-50.
51. Lasocka I, Jastrzębska E, Szulc-Dąbrowska L, Skibniewski M, Pasternak I, Kalbacova MH, et al. The effects of graphene and mesenchymal stem cells in cutaneous wound healing and their putative action mechanism. International Journal of Nanomedicine. 2019;14(null):2281-99.
52. Zhao M, Shi J, Cai W, Liu K, Shen K, Li Z, et al. Advances on Graphene-Based Nanomaterials and Mesenchymal Stem Cell-Derived Exosomes Applied in Cutaneous Wound Healing. International Journal of Nanomedicine. 2021;16(null):2647-65.
53. Akbarzadeh I, Saremi Poor A, Khodarahmi M, Abdihaji M, Moammeri A, Jafari S, et al. Gingerol/letrozole-loaded mesoporous silica nanoparticles for breast cancer therapy: In-silico and in-vitro studies. Microporous and Mesoporous Materials. 2022;337:111919.
54. He W, Wang Y, Li X, Ji Y, Yuan J, Yang W, et al. Sealing the Pandora's vase of pancreatic fistula through entrapping the digestive enzymes within a dextrorotary (D)-peptide hydrogel. Nature Communications. 2024;15(1):7235.
55. Cheng S, Yang J, Song J, Cao X, Zhou B, Yang L, et al. A motion-responsive injectable lubricative hydrogel for efficient Achilles tendon adhesion prevention. Materials Today Bio. 2025;30:101458.
56. Zhao J, Xu N, Niu B, Zhao X, Alorfix A. Dynamic event-triggered optimal control for stochastic interconnected nonlinear systems with matched disturbances via adaptive dynamic programming. Journal of the Franklin Institute. 2025;362(2):107360.
57. Kenry WCL, Loh KP, Lim CT. When stem cells meet graphene: opportunities and challenges in regenerative medicine. Biomaterials. 2018;155:236-50.
58. Zhang N, Zhang X, Zhu Y, Wang D, Liu W, Chen D, et al. MOF/MXene-loaded PVA/chitosan hydrogel with antimicrobial effect and wound healing promotion under electrical stimulation and improved mechanical properties. International Journal of Biological Macromolecules. 2024;264:130625.
59. Czarniewska E, Sielicki K, Maślana K, Mijowska E. In vivo study on borophene nanoflakes interaction with Tenebrio molitor beetle: viability of hemocytes and short-term immunity effect. Scientific Reports. 2023;13(1):11823.
60. Ahmed SR, Sherazee M, Das P, Shalauddin M, Akhter S, Basirun WJ, et al. Electrochemical assisted enhanced nanozymatic activity of functionalized borophene for H2O2 and tetracycline detection. Biosens Bioelectron. 2024;246:115857.
61. Mao L, Hu S, Gao Y, Wang L, Zhao W, Fu L, et al. Biodegradable and electroactive regenerated bacterial cellulose/MXene (Ti3C2Tx) composite hydrogel as wound dressing for accelerating skin wound healing under electrical stimulation. Advanced healthcare materials. 2020;9(19):2000872.
62. Faraji M, Arianpouya N. NiCoFe-layered double hydroxides/MXene/N-doped carbon nanotube composite as a high performance bifunctional catalyst for oxygen electrocatalytic reactions in metal-air batteries. Journal of Electroanalytical Chemistry. 2021;901:115797.

View Article Online
DOI: 10.1039/D5BM00609K

63. Parsaee F, Fayzullaev N, Nassar MF, Alreda BA, Mahmoud HMA, Taki AG, et al. Co-Fe dual-atom isolated in N-doped graphydine as an efficient sulfur conversion catalyst in Li-S batteries. Journal of Alloys and Compounds. 2024;988:174136.
64. Faraji M, Yousefi M, Yousefzadeh S, Zirak M, Naseri N, Jeon TH, et al. Two-dimensional materials in semiconductor photoelectrocatalytic systems for water splitting. Energy & Environmental Science. 2019;12(1):59-95.
65. Faraji M, Parsaee F, Kheirmand M. Facile fabrication of N-doped graphene/ $Ti_3C_2T_x$ (Mxene) aerogel with excellent electrocatalytic activity toward oxygen reduction reaction in fuel cells and metal-air batteries. Journal of Solid State Chemistry. 2021;303:122529.
66. Faraji M, Sabzali M, Yousefzadeh S, Sarikhani N, Ziashahabi A, Zirak M, et al. Band engineering and charge separation in the Mo1−xWxS2/TiO2 heterostructure by alloying: first principle prediction. RSC Advances. 2015;5(36):28460-6.
67. Faraji M, Yousefzadeh S, Nassar MF, Zahra MMA. $MnCo_2O_4$/N-doped graphene quantum dot vigorously coupled to MXene nanosheet: A bifunctional Oxygen electrocatalyst outperforms Pt/IrO_2 benchmark electrocatalysts in metal-air batteries. Journal of Alloys and Compounds. 2022;927:167115.
68. Adekoya GJ, Adekoya OC, Muloiwa M, Sadiku ER, Kupolati WK, Hamam Y. Advances In Borophene: Synthesis, Tunable Properties, and Energy Storage Applications. Small. 2024;20(40):2403656.
69. Mannix AJ, Zhou XF, Kiraly B, Wood JD, Alducin D, Myers BD, et al. Synthesis of borophenes: Anisotropic, two-dimensional boron polymorphs. Science. 2015;350(6267):1513-6.
70. Wang Z-Q, Lü T-Y, Wang H-Q, Feng YP, Zheng J-C. Review of borophene and its potential applications. Frontiers of Physics. 2019;14(3):33403.
71. Das P, Ganguly S, Marvi PK, Sherazee M, Ahmed SR, Tang X, et al. Borophene based 3D extrusion printed nanocomposite hydrogel for antibacterial and controlled release application. Advanced Functional Materials. 2024:2314520.
72. Das P, Ganguly S, Marvi PK, Sherazee M, Ahmed SR, Tang X, et al. Borophene Based 3D Extrusion Printed Nanocomposite Hydrogel for Antibacterial and Controlled Release Application. Advanced Functional Materials. 2024;34(21):2314520.
73. Chen SW, Huang SM, Wu HS, Pan WP, Wei SM, Peng CW, et al. A facile, fabric compatible, and flexible borophene nanocomposites for self-powered smart assistive and wound healing applications. Advanced Science. 2022;9(22):2201507.
74. Rao S, Sun Z, Liu Q, Cheng C, Jin C, Gao J, et al. Engineering atomic Ag1–N6 sites with enhanced performance of eradication drug-resistant bacteria over visible-light-driven antibacterial membrane. ACS nano. 2024;18(9):7074-83.
75. Zheng Y, Cai X, Chen G, Xiang D, Shi W, Shen J, et al. Single Atom-Dispersed Silver Incorporated in ZIF-8-Derived Porous Carbon for Enhanced Photothermal Activity and Antibacterial Activities. International Journal of Nanomedicine. 2024:4253-61.
76. Zhang S, Ruan W, Guan J. Single-atom nanozymes for antibacterial applications. Food Chemistry. 2024:140094.
77. Dai S, Yao L, Liu L, Cui J, Su Z, Zhao A, et al. Carbon dots-supported Zn single atom nanozymes for the catalytic therapy of diabetic wounds. Acta Biomaterialia. 2024;186:454-69.
78. Qiu X, Zhuang L, Yuan J, Wang H, Dong X, He S, et al. Constructing multifunctional Cu Single-Atom nanozyme for synergistic nanocatalytic Therapy-Mediated Multidrug-Resistant bacteria infected wound healing. Journal of Colloid and Interface Science. 2023;652:1712-25.
79. Li Z, Xu D, Deng Z, Yin J, Qian Y, Hou J-T, et al. Single-Atom-Catalyzed MXene-Based nanoplatform with Photo-Enhanced Peroxidase-Like activity nanotherapeutics for Staphylococcus aureus infection. Chemical Engineering Journal. 2023;452:139587.

View Article Online
DOI: 10.1039/D5BM00609K

80. Dai X, Liu H, Cai B, Liu Y, Song K, Chen J, et al. A Bioinspired Atomically Thin Nanodot Supported Single-Atom Nanozyme for Antibacterial Textile Coating. Small. 2023;19(47):2303901.
81. Göktuna S, Taşaltın N. Preparation and characterization of PANI: α borophene electrode for supercapacitors. Phys E. 2021;134:114833.
82. Aslam S, Isab AA, Alotaibi MA, Saleem M, Monim-ul-Mehboob M, Ahmad S, et al. Synthesis, spectroscopic characterization, DFT calculations and antimicrobial properties of silver (I) complexes of 2, 2'-bipyridine and 1, 10-phenanthroline. Polyhedron. 2016;115:212-8.
83. Fan L, Yang H, Yang J, Peng M, Hu J. Preparation and characterization of chitosan/gelatin/PVA hydrogel for wound dressings. Carbohydrate polymers. 2016;146:427-34.
84. Lashaki RA, Raeisi Z, Razavi N, Goodarzi M, Najafzadeh H. Optimized classification of dental implants using convolutional neural networks and pre-trained models with preprocessed data. BMC Oral Health. 2025;25(1):535.
85. Wang Y, Xiao D, Yu H, Ke R, Shi S, Tang Y, et al. Asymmetric composite wound dressing with hydrophobic flexible bandage and tissue-adhesive hydrogel for joints skin wound healing. Composites Part B: Engineering. 2022;235:109762.
86. Yin M, Wang X, Yu Z, Wang Y, Wang X, Deng M, et al. γ-PGA hydrogel loaded with cell-free fat extract promotes the healing of diabetic wounds. Journal of Materials Chemistry B. 2020;8(36):8395-404.
87. Shi Y, Ma C, Peng L, Yu G. Conductive "smart" hybrid hydrogels with PNIPAM and nanostructured conductive polymers. Advanced Functional Materials. 2015;25(8):1219-25.
88. Atila D, Karataş A, Keskin D, Tezcaner A. Pullulan hydrogel-immobilized bacterial cellulose membranes with dual-release of vitamin C and E for wound dressing applications. International Journal of Biological Macromolecules. 2022;218:760-74.
89. Dai T, Wang C, Wang Y, Xu W, Hu J, Cheng Y. A nanocomposite hydrogel with potent and broad-spectrum antibacterial activity. ACS applied materials & interfaces. 2018;10(17):15163-73.
90. Corcoran M, Morris D, De Lappe N, O'connor J, Lalor P, Dockery P, et al. Commonly used disinfectants fail to eradicate Salmonella enterica biofilms from food contact surface materials. Applied and environmental microbiology. 2014;80(4):1507-14.
91. Fayzullaev N, Keshavarz M, Omidi M, Rakhimov S, Nazirova R, Mohealdeen SM, et al. Enhancing Li-S Battery Performance by Harnessing the Power of Single Atoms on 2D Borophene. Electrochimica Acta. 2025:145831.
92. Wang W, Yu Z, Alsammarraie FK, Kong F, Lin M, Mustapha A. Properties and antimicrobial activity of polyvinyl alcohol-modified bacterial nanocellulose packaging films incorporated with silver nanoparticles. Food Hydrocolloids. 2020;100:105411.
93. Sharafkhani F, Corns S, Holmes R. Multi-Step Ahead Water Level Forecasting Using Deep Neural Networks. Water. 2024;16(21):3153.
94. Yin B, Gosecka M, Bodaghi M, Crespy D, Youssef G, Dodda JM, et al. Engineering multifunctional dynamic hydrogel for biomedical and tissue regenerative applications. Chemical Engineering Journal. 2024;487:150403.
95. Samawi KA, Abdulrazzaq SJ, Zorah M, Al-Bahrani M, Mahmoud HMA, Abdulkareem-Alsultan G, et al. MoS_2/graphdiyne nanotube/MXene 3D-interconnected ternary aerogel: A high-performance electrocatalyst for hydrogen evolution reaction. Journal of Solid State Chemistry. 2024;334.
96. Dizayee W, Hamarashid MM, Zorah M, Mahmoud HMA, Al-Bahrani M, Taki AG, et al. Synergistic effect of $Ni(OH)_2$ and MXene nanosheets in 3D framework on the improvement of dielectric, energy storage, mechanical and thermal characteristics of polyvinylidene fluoride(PVDF) polymeric composites. Journal of Alloys and Compounds. 2024;1004.

View Article Online
DOI: 10.1039/D5BM00609K

97. Abd-Alkuder Salman E, Abaid Samawi K, Fawzi Nassar M, Abdulkareem-Alsultan G, Abdulmalek E. 3D Hollow Spheres Comprising MXene/g-C_3N_4 Heterostructre for Efficient Polysulfide Adsorption and Conversion in High-Performance Li-S Batteries. Journal of Electroanalytical Chemistry. 2023:117629.
98. Xu TT, Zheng J-G, Wu N, Nicholls AW, Roth JR, Dikin DA, et al. Crystalline boron nanoribbons: synthesis and characterization. Nano Letters. 2004;4(5):963-8.
99. Faraji AR, Khoramdareh NB, Falahati F, Jafari S, Monfared SA, Faghih A. Superparamagnetic MnFe alloy composite derived from cross-bindered of chitosan/rice husk waste/iron aluminate spinel hercynite for rapid catalytic detoxification of aflatoxin B1: Structure, performance and synergistic mechanism. Int J Biol Macromol. 2023;234:123709.
100. Jebelli F, Hasheminejad H, Felegari N. Efficiency assessment of permeable reactive barriers for methyl tert-butyl ether (MTBE) remediation in groundwater using novel adsorbents: Aerogel, sillimanite, andalusite, and tourmaline - Insights from batch and column studies. Case Studies in Chemical and Environmental Engineering. 2024;10:100962.
101. Faraji AR, Ramazi Farahani A, Bakhsi Khoramdareh N, Gil A, Jafari S, Hekmatian Z, et al. Cu-Fe nanoparticles decorated rice hull/chitosan@FeAl2O4 to boosted peroxidase-like activity for catalytic degradation of antibiotics: Kinetics and mechanistic insights. Journal of Environmental Chemical Engineering. 2023;11(6):111348.
102. Li Z, Fu J-Y, Feng Y, Dong C-K, Liu H, Du X-W. A silver catalyst activated by stacking faults for the hydrogen evolution reaction. Nature Catalysis. 2019;2(12):1107-14.
103. Feng J, Fan D, Wang Q, Ma L, Wei W, Xie J, et al. Facile synthesis silver nanoparticles on different xerogel supports as highly efficient catalysts for the reduction of p-nitrophenol. Colloids and Surfaces A: Physicochemical and Engineering Aspects. 2017;520:743-56.
104. Khan S, Ranjha NM. Effect of degree of cross-linking on swelling and on drug release of low viscous chitosan/poly (vinyl alcohol) hydrogels. Polymer bulletin. 2014;71:2133-58.
105. Shelma R, Sharma CP. Development of lauroyl sulfated chitosan for enhancing hemocompatibility of chitosan. Colloids and Surfaces B: Biointerfaces. 2011;84(2):561-70.
106. Krishnamurthi VR, Rogers A, Peifer J, Niyonshuti II, Chen J, Wang Y. Microampere electric current causes bacterial membrane damage and two-way leakage in a short period of time. Applied and environmental microbiology. 2020;86(16):e01015-20.
107. Eom S-H, Lee D-S, Jung Y-J, Park J-H, Choi J-I, Yim M-J, et al. The mechanism of antibacterial activity of phlorofucofuroeckol-A against methicillin-resistant Staphylococcus aureus. Applied microbiology and biotechnology. 2014;98:9795-804.
108. Viola SG, Dalmolin LF, Muñoz JBV, Martins YA, dos Santos Ré AC, Aires CP, et al. Investigation of the antimicrobial effect of anodic iontophoresis on Gram-positive and Gram-negative bacteria for skin infections treatment. Bioelectrochemistry. 2023;151:108374.

View Article Online
DOI: 10.1039/D5BM00609K

Data are available upon request.